

Chapter 13

Nanostructured Catalysts

Martin Schmal and Silvia Moya

Abstract Nanostructured systems are of great interest from points of view of basic science and technological applications. Within the topic of catalysis, should be highlighted the properties associated with different morphologies, activities and selectivities, which are strongly affected by the shape and particle size; in the case of crystalline metallic phases are oriented crystal faces. The reactions that are influenced by these factors (morphological) are known as structure sensitive reactions.

Keywords Grapheme • Metals • Nanostructure • NCT • Oxides

13.1 Part I: Introduction

Nanostructured systems are of great interest from points of view of basic science and technological applications. Currently, in general, any material that contains grain clusters, plates, or filament size smaller than 10 nm can be regarded as nanostructure, as long as their properties differ from those of the bulk solids. These materials have been extensively studied in recent years, because the small size (particles, grains, or phases) and high surface/volume ratio (S/V) resulted in mechanical, optical, electronic, and natural magnetic properties in important applications.

In the transition metal nanoparticles, new behaviors arise deriving from effects related to the size reduction. Changes in its electronic structure provide the development of new reactivity characteristics, in addition to other previously cited properties with respect to those presented by the bulk structure. These behaviors are also related to surface effects as superplasticity, dynamic differential sintering, and catalysis.

The size and surface characteristics are related through the S/V ratio. For spherical particles, the S/V ratio is inversely proportional to its radius R , ($S/V = 3/R$). Clusters of type complete layer (full shell) are formed with atoms packed in closed hexagonal structure (hcp) and cubic (ccp). This model assumes that the particles are constructed by adding densely packed layers around a central atom. The number of atoms per layer is represented by $N_s = 10n^2 + 2$, where n is the layer number in question. The total number of atoms (N) in a structure consisting of N layers is $N = (10n^3 + 15n^2 + 11n + 3/3)$. The S/V ratio can be






Full-Shell "Magic Number" Clusters					
Number of shells	1	2	3	4	5
Number of atoms in cluster	M_{13}	M_{55}	M_{147}	M_{309}	M_{561}
Percentage surface atoms	92%	76%	63%	52%	45%

Fig. 13.1 Scheme of cluster-type full-layer hexagonal packing (Adapted from Aiken, *J. Mol. Catal. A*, vol. 145, pp. 1–44, 1999)

obtained, so the ratio of surface atoms to the total atoms constituting the cluster, N_s/N [1, 2].

Most of these clusters assume complete layer structures, as shown in Fig. 13.1, since the optimal number of metal–metal atom bonds for each leads to higher stabilization of the system.

This configuration allows higher stability of the clusters; it provides a structure whose atoms have the largest possible number of neighbors. The cluster growth decreases the amount of surface atoms [1, 2].

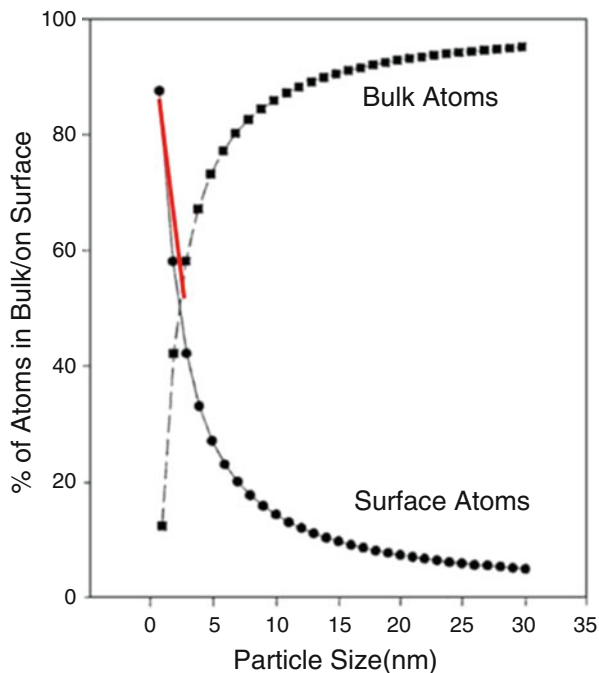
In a few hundred of nano atoms, the major fraction of them is located at the surface. Because of the tendency that surface atoms are coordinately unsaturated, high surface energy has great contribution to the total energy of the system. Also, a high ratio S/V , that is, the particle size and its shape, influences the electronic structure of cluster levels. These properties have been reported in the literature in different aspects of nanoscience.

Within the topic of catalysis, the properties associated with different morphologies, activities, and selectivities should be highlighted, which are strongly affected by the shape and particle size; in the case of crystalline, metallic phases are oriented crystal faces. The reactions that are influenced by these factors (morphological) are known as structure-sensitive reactions. The high performance of nanostructured catalysts is explained by the high concentration of atoms at the surface, due to the small particles. The variation of surface atoms relative to the solid volume, as a function of particle size, is illustrated in Fig. 13.2.

Note that the percentage of surface atoms increases the smaller the particle size and decreases with increasing particle size. But the opposite is true in the bulk, indicating that the larger the size of particles, the greater the concentration of atoms in the bulk phase. Catalytic reactions are surface phenomena, and the size reduction of the active phase may favor them as follows:

- The reactions occur at lower temperatures due to the high ratio of surface atoms/volume changes in the electronic levels.
- Increased yield and selectivity due to greater surface active area available and morphology.
- Increased mechanical strength.

Fig. 13.2 Surface atoms versus bulk atoms (Adapted from Aiken 1999, *J. Mol. Catal. A*, vol. 145, pp. 1–44, 1999; Burda et al. *Chem. Rev.*, vol. 105, pp. 1025–1102, 2005)



There are excellent reactivity characteristics, as a result of the decreasing size high surface/volume ratio, compared to bulk materials.

It is well known from studies of model catalysts (single crystal), under conditions of ultrahigh vacuum (UHV), that the selectivity is significantly influenced by the crystal face. The catalytic activity of metal nanoparticles of different shapes was quite reasonably correlated with the fraction of atoms located at vertices and edges of the crystalline metal structures [3]. Its unique properties associated with the ability to synthesize in different size ranges and shapes make these materials potentially useful in catalysis, which are more active and selective than the conventional catalysts.

Nowadays, materials which are of great interest are the carbon nanotubes (CNT) and graphene, which were invented the first time in (1962) and present new properties which can be applied in catalysis [4]. They present high chemical resistivity and are resistant to oxidation and to temperatures. CNT presents electric transport like metals, semiconductors, or superconductors, besides mechanical resistance and flexibility, which can be applied in sensors, polymers, ceramics, and of course catalysis, in particular for hydrogen storage and fuel cells [5].

13.1.1 Synthesis of Nanostructured Catalysts

The syntheses of nanostructured materials are of different natures, such as:

- Metals
- Oxides

- Sulfites or carbides
- Carbon nanotubes and oxide nanotubes
- Nanostructured oxides and mixed oxides

Nanostructured materials for metals or supported oxides, oxides and mixed oxides, and in particular graphenes will be focused. The most important requirements that should guide the choice of a method of synthesis for these classes of materials are:

- Control of particle size
- Control of the particle size distribution
- Control of morphology or particle shape
- Homogeneous distribution of particulate material supported thereby including the largest number of surface active sites available for reaction, adsorption, etc.

There are several routes that can be chosen for the synthesis of nanostructured systems. The method may involve the preparation of novel compounds from a precursor that is called chemical synthesis or may involve only a vaporization process and cooling the material under controlled condensation conditions; it is classified as physical preparation.

The *physical methods* of preparation of nanostructured materials are basically of gas phase synthesis, which allows getting a flexible composition and a high degree of homogeneity in the generation of “nanoclusters,” ranging from refractory materials to multicomponent alloys. The following are among the physical methods that are noteworthy:

- Chemical vapor deposition (CVD) or sputtering
- Lithography by electron beam
- Plasma

Chemical methods, on the other hand, exert the main role in the synthesis of nanomaterials. The advantage of chemical synthesis methods is the variety of methods and versatility in the design characteristics such as structures and compositions, in addition to increased operational simplicity. The materials obtained by chemical processes have greater homogeneity, because the chemical synthesis allows interaction between the components of the reaction mixture at the molecular scale. Consequently, understanding how matter interacts and organizes this dimension allows the understanding of its effect on the macroscopic properties of the desired products. Figure 13.3 shows a general scheme of nanomaterial synthesis.

Among the chemical methods, we have [1, 6]:

- In situ precipitation of metal precursors
- Synthesis in confined spaces—microemulsion
- Sonochemical synthesis
- Deposition–precipitation
- Sol–gel method
- Thermal decomposition

Nanostructured Catalysts - Synthesis

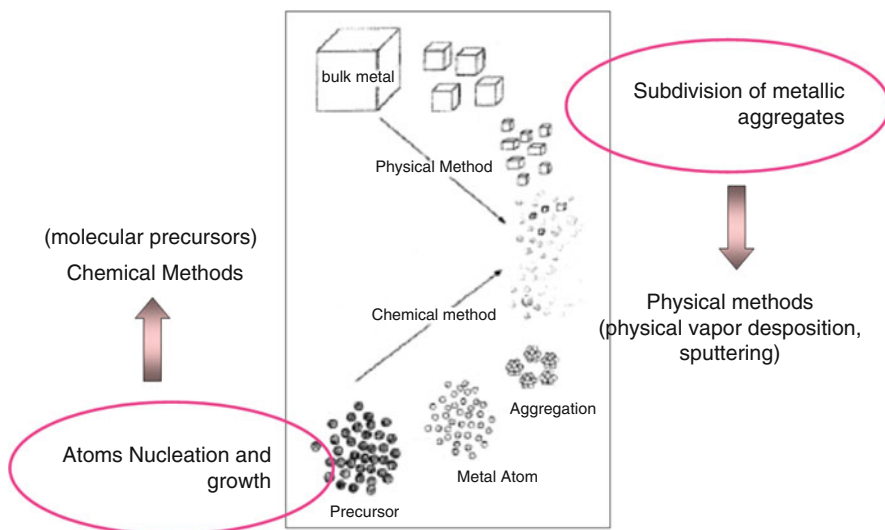


Fig. 13.3 Schematic representation of physical and chemical methods

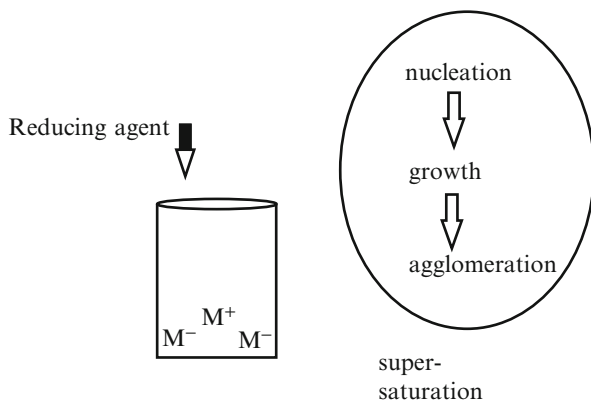
- Photochemical synthesis
- Reduction or decomposition of binders of organometallic compounds
- Chemical vapor decomposition

13.1.2 *In Situ Precipitation of Metal Precursors*

The precipitation process is basically a nucleation followed by growth and agglomeration of poorly soluble products generated in supersaturation condition. To obtain nanostructured materials, one must control the growth stage and prevent agglomeration in the reaction medium, which may be aqueous or organic. As in most precipitation processes, the supersaturation condition must be reached; in this case, the reduction of the metal precursor is obtained by adding a reducing agent which is added to the reaction medium. Figure 13.4 shows a simplified scheme of synthesis of precipitation conditions.

In the precipitation method, one should pay attention on the choice of the parameters for controlling the precipitation reactions for the increased growth of the particles of desired characteristics (size and morphology). The first step is the nucleation, which must occur at a high degree of supersaturation of the solution, in order to form a large number of nucleation centers (very small crystals), in a short period of time. To ensure uniformity in size of the crystals, it is necessary that only the nuclei are formed in the first stage and then should only grow via molecular mechanisms until the precipitate of the equilibrium concentration is achieved.

Fig. 13.4 Scheme of the precipitation method



The reaction for extended periods of time can result in the total reagent shortage. Thereafter, in the period called aging reaction, begins the digestion of solid formed. The digestion of the precipitate occurs with the growth of larger particles due to the consumption of the smaller particles which decrease in size until complete dissolution, in a process known as Ostwald digestion [2]. This process also leads to the formation of larger particles and a solution with broad size distribution.

Deposition on Supports

The deposition of the active phase on a support depends on the surface charges of the support and of precursor in suspension. The surfaces of the particles in a polar medium develop loadings caused by ionization process in which functional groups are present in the material or even ionized by the ion adsorption. This affects the distribution of the charge near ions, increasing the concentration of counter ions near the surface. Thus, an electrical potential is generated, which decreases exponentially away from the surface, as expressed by Eq. (13.1). The adsorbed ions cause decreasing electric potential, as illustrated in Fig. 13.5a:

$$\psi = \psi_0 \cdot e^{-\kappa \cdot x} \quad (13.1)$$

where ψ is the electric potential at a distance x from the surface, ψ_0 is the potential on the particle surface, and κ is the Boltzmann constant ($\kappa = 1.38 \cdot 10^{-23} \text{ J / K}$).

The adsorption of charged ions on the surface leads to the formation of the so-called electrical double layer, which can be divided into two regions, the Stern layer and the diffusion layer as shown in Fig. 13.5a. The Stern layer indicates ions strongly adsorbed at the surface, while the diffusion layer is a region in which the distribution of the ions is determined by the balance between the electrostatic forces and thermal motion.

This phenomenon is known as electrophoresis. The particles and ions strongly adsorbed (Stern layer) move as a unit, and the electric potential at the border of the unit where the sliding takes place between the phases is known as the zeta potential (Setz 2009). The zeta potential is influenced by the pH of the system since the H^+ and OH^- ions affect the surface charge of the particle and thus the zeta potential

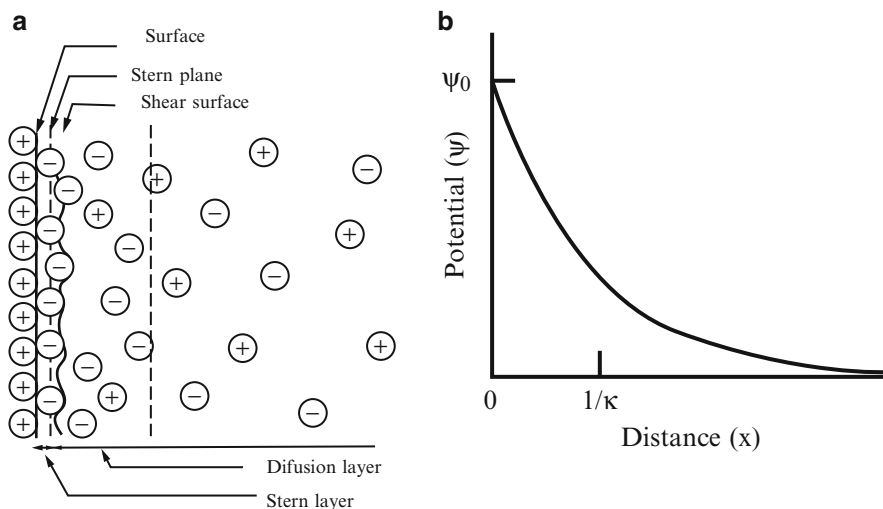


Fig. 13.5 (a) Representation of the electric double layer in a positively charged surface; (b) the variation of the electric potential as a function of distance from the surface positively charged. The variable $1/\kappa$ is called the “thickness of the electrical double layer” (Adapted from Roucoux A., Schulz J., Patin H., *Chem. Rev.*, vol. 102, pp. 3757–3778, 2002) [7]

(Adamson 1997). The pH value of suspension at which the zeta potential is zero is known as the isoelectric point (IEP). In this case, the electrostatic repulsion between particles is negligible, and van der Waals forces act to promote the approach of the ions and subsequently the coagulation. Where both the zeta potential of the particle as the surface load is null, there is the so-called point of zero charge (PZC). This can be performed using the zeta potential analyses (IEP) in order to promote greater electrostatic interaction between the support and the precursor of the active phase, allowing better adherence of the active phase.

Figure 13.6 illustrates the behavior of the alumina surface at different pH values. Note that at pH values below 13 (PIE alumina), its surface becomes positively charged due to exposure OH_2^+ groups. At pH 13, the alumina is electrically neutral, and at higher values, it is negatively charged.

13.1.3 Synthesis of Stabilized Nanoparticles: Colloidal Nanoparticles

Virtually, all grades of colloidal inorganic nanocrystal well-defined structure may be synthesized by a variety of methods, including [8]:

- Coprecipitation in aqueous phase
- Power coprecipitation

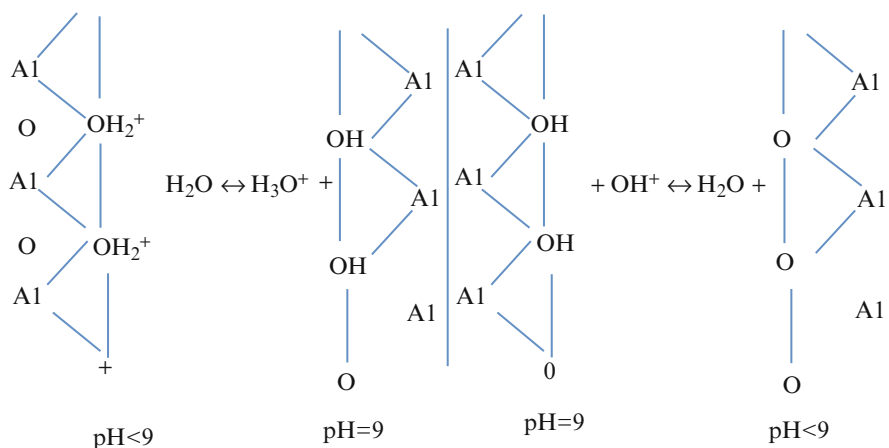


Fig. 13.6 Hydrated alumina surface at different pH values

- Microemulsion
- Hydrothermal and thermal–solvent synthesis

The usual route for the preparation of colloidal nanoparticles is the precipitation. The production of stabilized metal nanoparticles requires the reduction in aqueous or organic solution, in the presence of a stabilizing agent. The main components of systems for the synthesis of colloidal nanoparticles are:

- Metallic precursor
- Reducing agent (alcohol, H₂, hydrates, NaBH₄)
- Stabilizing agent (organic/inorganic binders, polymers, and surfactants)

There are two ways for stabilization of nanoparticles:

- *Electrostatic*: as a result of adsorption of ions (most commonly chloride, hydroxide and hydronium) on the surface of the nanoparticle forming a double layer (EDL)
- *Spatial repulsion*: due to species with long organic chains that involve metallic particle, which is the most common

Figure 13.7 shows schematically both ways of stabilizing colloidal nanoparticles.

The stabilization using inorganic colloid method is limited to aqueous solutions and some polar protonic solvents. Due to the dynamic nature of the electrical double layer (EDL), these systems are extremely susceptible to environmental conditions (temperature, concentration, pH), reducing considerably its stability compared to other forms of stabilization.

According to another way of stabilizing colloids, the presence of bulky organic chains around the nanoparticles prevents agglomeration due to van der Waals force interparticle. The organic interface (hydrophilic or hydrophobic character) colloid stabilizes both in water and in nonpolar solvents. The steric stabilization is the most

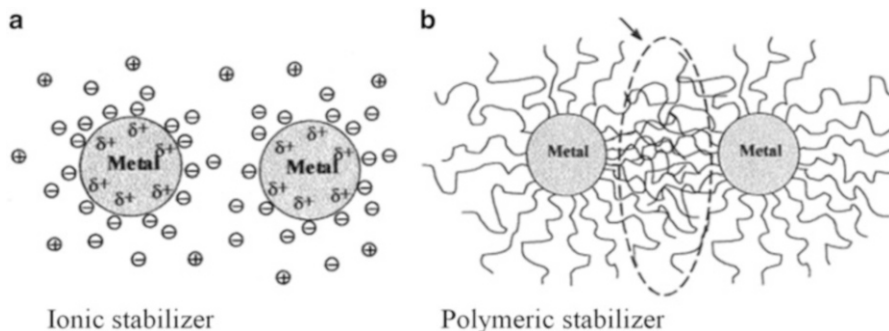


Fig. 13.7 Scheme of stabilizing nanoparticles: (a) DCE; (b) Spatial repulsion (Adapted from Novoselov, *Nature Materials* 6 (2007) 183–191). (a) Ionic stabilizer. (b) Polymeric stabilizer

common due to the colloid stability characteristics in wide pH ranges and in solvents of different polarities [9]. A variety of compounds are used as stabilizers. The most effective agents in the stabilization of inorganic colloids are surfactants or polymer-coordinating ligands or “capping ligands”. All these substances must have polar groups (electron density donors), as phosphines [10], carboxylates [11] [190], sulfates [12, 13] [48], neutral amines [14] [232], and nitrogen heterocycles [15] [23]. These groups interact with the surface of nanoparticles in order to coordinate to metal atoms surface electron deficient. The organic chain-extending molecule provides physical isolation of the solvent and governs the nanocrystal solubility properties of the material.

Characteristics such as particle diameter, morphology, and size distribution are strongly influenced by the composition of the precursor solution during the precipitation.

So important as the nature of the reducing agent and reaction conditions are the type and amount of the stabilizer to obtain specific morphological properties. Besides, the manipulation of the concentration of the metallic precursor relative to the stabilizer is another way to control size of nanoparticles. The high-ratio stabilizer/metal cations lead to the formation of smaller crystallites during nucleation. During growth, the binder adsorbs reversibly at the particle surface and in the case of stabilization, by space constraints, produces a dynamic organic coating which stabilizes crystals in solution mediating growth. Larger molecules provide greater shielding nanoparticle, resulting in a smaller average size of the system.

Impregnation on the Support

The nanoparticles can be used as catalysts in liquid phase or impregnated on supports. In this case, it follows by drying, calcination, and activation steps.

In gas–solid catalytic systems, the precursor of the catalyst previously supported passes through the calcination process, owing to the shielding around the metal particles, so that the metal layer can be exposed to the reactants. The use of binders with low decomposition temperatures permits the removal of stabilizers which can be carried out under mild temperature conditions and does not cause damage to the

particle structure. It is extremely important that the calcination procedure impedes the formation of carbon deposits on the surface, blocking active sites.

Influence of Temperature on Supported Nanoparticles

Wang et al. [8] studied the thermal behavior Pt supported on SiO_2 amorphous nanocrystals in a transmission electron microscope in situ reaction chamber. The authors followed the heating process performed in the microscope and observed that increasing the temperature above $350\text{ }^\circ\text{C}$ induces morphological deformation of nanocrystals. The continuous heating promotes fusion of the surface of the nanoparticles and their spreading on surface of the carrier rather than the sintering material inducing the change in the morphology thereof. In Fig. 13.8 it is possible to observe this process. When the particles are close enough, the coalescence becomes unavoidable Fig. 13.8.

El-Sayed [16] observed through TEM in situ the images of Pt nanocrystals at different temperatures, as shown in Fig. 13.9. The triangular shapes are preserved at temperatures up to $350\text{ }^\circ\text{C}$, without truncation of vertices and edges. The morphology changed from triangular shape to the spherical at $500\text{ }^\circ\text{C}$, due to melting of surface atomic layers; however, the inner particle maintains the

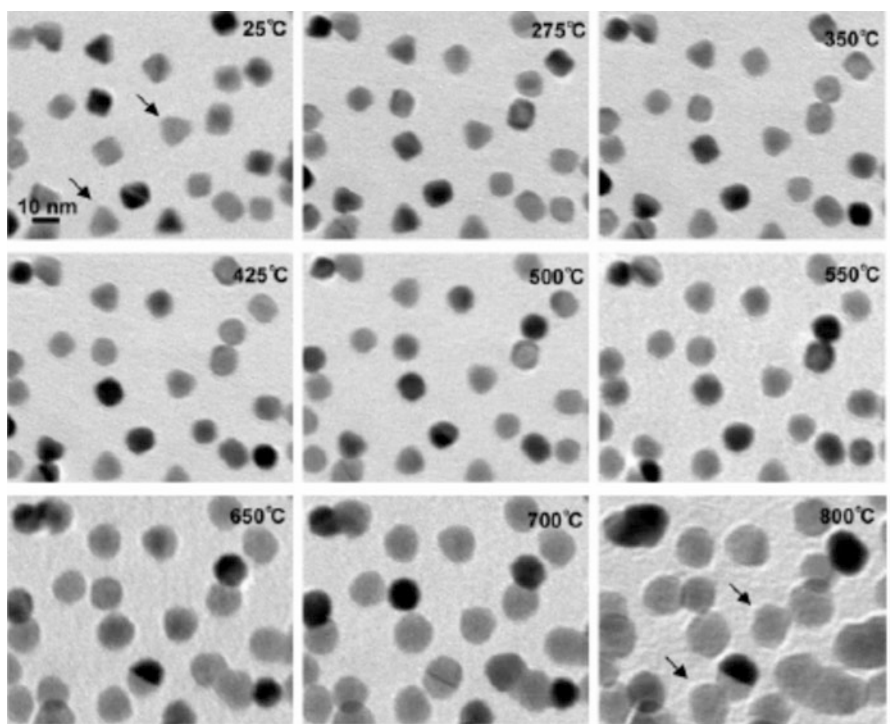


Fig. 13.8 Micrographs from TEM of the Pt/SiO₂ in situ treatment with increasing temperature, cubic and tetrahedral particles (Wang X., Zhuang J., Peng Q., Li Y., *Nature*, vol. 437, pp. 121–124, 2005, reproduced with permission)

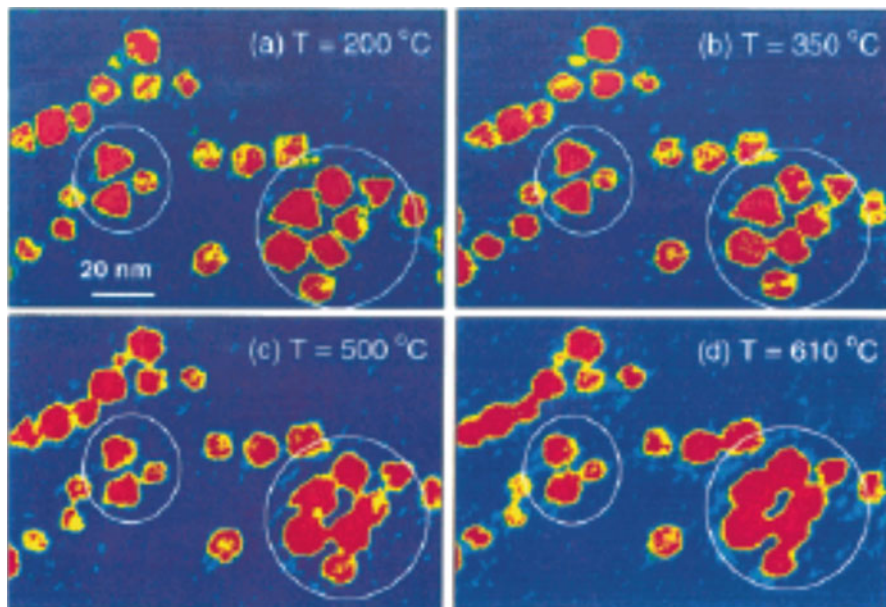


Fig. 13.9 TEM in situ images of Pt nanocrystals at different temperatures (El-Sayed M. A., *Acc. Chem. Res.*, vol. 34, 257–264 (2001) reproduced with permission)

crystalline structure. The fusion at 600 °C becomes clear, leading to coalescence of the particles. Authors also observed differences in the stability of the different morphologies and concluded that the tetrahedral particles were the most stable, followed by the cubic and the triangular shapes [8, 16].

The regions marked with small circles represent changes of shape, and nanocrystals marked by large circles represent the merger of the crystals of the group. The blue color represents the background of the substrate, red the approximate projection of higher atomic density region of Pt, and yellow the projection of lower atomic density [8, 16].

13.1.4 Metal Nanostructures [8, 17–53]

Clusters, grains, lamellar structures, or filaments with dimensions smaller than 10 nm can be considered as nanostructured materials. These systems present a high ratio of surface area and volume with singular properties. In catalysis, changes in the surface and bulk electronic structure, caused by nanostructuring, may influence the reactivity, causing it to differ substantially from the conventional systems. Therefore, structure-sensitive reactions are strongly influenced by particle sizes

and, thus, on the method of preparation of the supported metal catalyst [30, 54], for example, in the FT synthesis, using Fe/SiO₂.

Nanoparticles of Pd supported on Al₂O₃ were synthesized by Okitsu et al. [55] using as precursor (PdCl₄)²⁻. The authors claim that the particles supported were first nucleated as reduced Pd species, followed by growth in the solution, and finally anchoring on the support. Compared to the conventional impregnation method of preparation, the activity for hydrogenation was 20 times better.

Colloidal Method

Miyazaki et al. [56] prepared Pt nanoparticles using *colloids* with different morphologies, using K₂PtCl₄ in the presence of hydrogen and three different stabilizers, and obtained nanocrystallites of average diameters of 6.13 nm, 13.6 nm, and 13.6 nm, using also polyvinylpyrrolidone (PVP) polymer, poly(*N*-isopropylacrylamide polymer) (PNIPA), and sodium polyacrylate (SPA), respectively. As observed, there are great differences between particle sizes and morphologies. Duteil et al. [57] synthesized nickel particles stabilized by colloidal phosphines from Ni (acac) 2 (nickel acetylacetonate, C₁₀H₁₃NiO₄) in diethyl ether solutions using diethyl aluminum hydride as a reducing agent at -40 °C and obtained particles with an average diameter of 4 nm order. Miyazaki et al. [56] obtained particles on the order of 7–15 nm, using polyvinylpyrrolidone (PVP), poly(*N*-isopropylacrylamide) (PNIPA), and sodium polyacrylate (SPA), as stabilizers, respectively, as shown in Fig. 13.10.

Besides the difference between the observed particle sizes, its shape was greatly altered. Figure 13.10 gives the morphology of the synthesized materials [56].

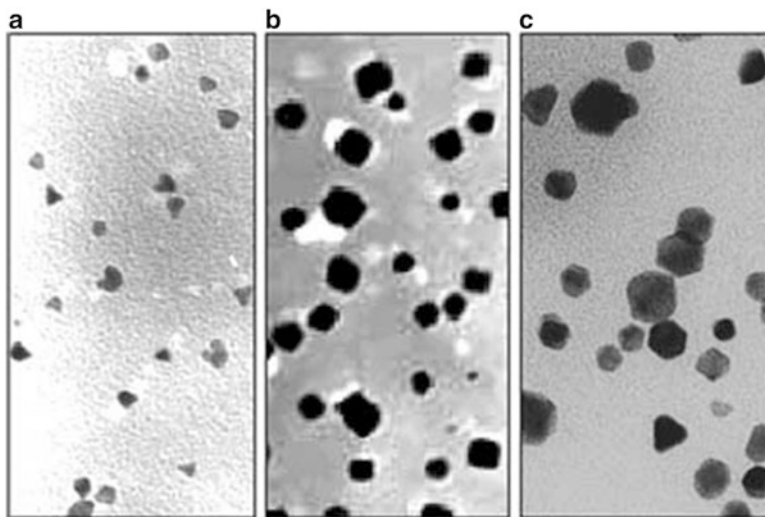


Fig. 13.10 Pt nanoparticles using different stabilizers (Miyazaki A., Balint I., Nakano Y., *J. Nanop. Res.*, vol. 5, pp. 69–80, 2003, reproduced with permission)

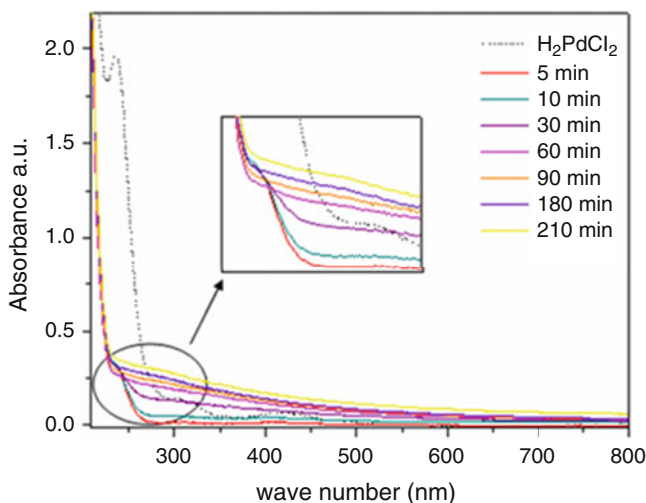


Fig. 13.11 UV-Vis spectra during reduction of Pd forming colloidal solution [17]

The Pd catalysts supported on α - Al_2O_3 using the colloidal method was also prepared by the colloidal method. The reduction of transition metals with ethanol is a widely used method for producing colloidal nanoparticles. In this process, ethanol acts both as a solvent and as a reducing agent. During the reduction, the alcohol is oxidized to aldehyde, yielding acetaldehyde. The reduction of Pd to the formation of the nanoparticles was monitored by spectroscopy in the UV-Vis region, which showed a rapid decrease of the concentration of Pd^{+2} ions from the solution as a result of the reduction process for the formation of the metal colloid. The solution prior to refluxing showed pale yellow color with a peak in the UV-Vis spectrum at 235 nm, a band that can be attributed to absorptions for the transfer of load from the binder metal ions $[\text{PdCl}_4]^{2-}$, as shown in Fig. 13.11. It was also observed by the color change from pale yellow to brown solution [19, 29].

The solution was analyzed by transmission electron microscopy, and the results are shown in Fig. 13.12. It was found in this case that the synthesis has led to obtain a solution having a large size distribution with dimensions ranging between 2 nm and 20 nm. The particles have not yet submitted various morphologies; particles were found from so close to spherical and even cubic tetrahedral triangular with maximum size limited to less than 20 nm, due to the action of the stabilizing polymer.

This solution was impregnated on α - Al_2O_3 and submitted to the usual pretreatment conditions. During the impregnation process and drying, the stabilizer was not decomposed, being submitted to calcination to remove the PVP, such that the metal is located at the external surface of the support. Figure 13.13 shows the images of the sample after calcination and reduction. There is a tendency of aggregating particles on the surface. This behavior is frequently seen on highly

Fig. 13.12 Micrograph of a colloidal solution of palladium [11]

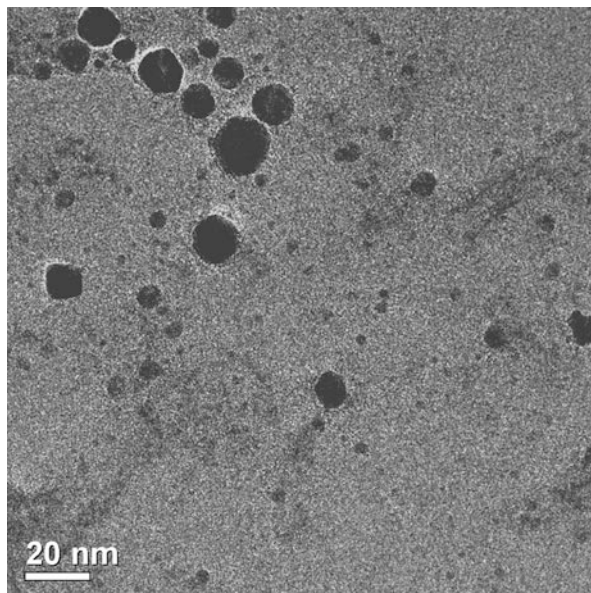
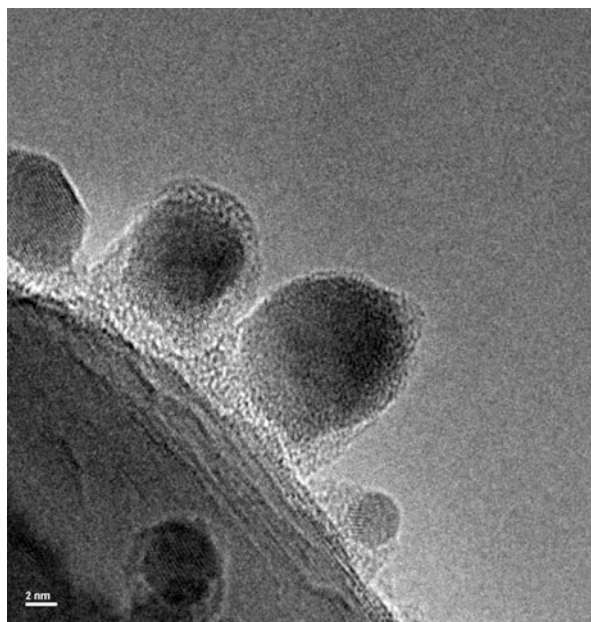


Fig. 13.13 Micrograph of TEM image of the palladium catalyst after calcination and reduction. Scale bar, 2 nm [18]



dispersed metal particles, because in nanometric scale the surface energy is high and tends to aggregate, decreasing the total energy. It is possible to see a trend of clustering of the particles on the surface of alumina. These clusters are made up of several metallic particles down to 10 nm.

Sonochemical Method

The *sonochemical* term is used to describe the use of ultrasound as a preparation tool. Ultrasound makes up a region of the electromagnetic spectrum between the frequencies of 20 kHz to 1000 MHz.

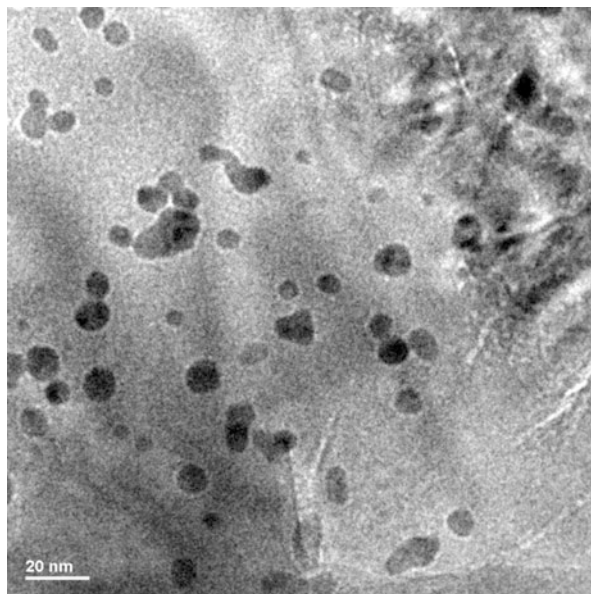
The synthesis of nanostructured inorganic materials by sonochemical had already been synthesized a large number of nanostructures of different compositions with comparable or better than the properties of the same when summed with other preparation methods. The versatility of this method also extends to the relative flexibility of reaction conditions such as the nature of the precursors and their solutions, the possibility of addition of auxiliaries, and the presence of “traps” (species immobilized) to the nanoparticles. All types of metallic nanostructured materials synthesized by *sonochemical* described (powders, colloids, or nanoparticles supported) can also be obtained for other classes of compounds such as oxides [58–60], sulfides [61], Suslick [20, 62], and more recently selenides [63, 64] and tellurides [65].

The acoustic cavitation phenomenon is responsible for disturbances caused by the components of a liquid medium during sonication. This phenomenon is the formation, growth, and implosive collapse of microbubbles associated with the propagation of sound waves in the liquid medium. The sound is transmitted via a fluid like a wave alternated with periods of compression and rarefaction. Cavitation is a result of the overlap of the sinusoidal sound pressure with the constant pressure of the medium. During periods of negative pressure (rarefaction wave period), the expanding gas is dissolved in solution (and volatile components) for the formation of microbubbles. The growth of the bubble extends to a distance many times greater than their nucleation radius. When its maximum distance is reached, immediately before the collapsing, the internal pressure becomes lower than the pressure of the liquid medium, resulting in an implosion. At this time, the acoustic pressure amplitude is maximum, the period of bubble compression by the wave sound [66].

The sonochemical method is similar to the precipitation process, using a metal precursor solution (ionic), a reducing agent, and a compound that prevents agglomeration which is a molecular stabilizer and/or a support.

Okitsu et al. [55], carried out the sonochemical synthesis of crystalline nanoparticles of Au, Ag, Pd, and Pt stabilized with polyethylene glycol monostearate (MS-PEG), sodium dodecyl sulfate (SDS, $\text{NaC}_{12}\text{H}_{25}\text{SO}_4$), and polyvinylpyrrolidone (Okitsu 1996a, b) [233, 234]. The metal particles were produced from 5 nm order and are stable for months.

Fig. 13.14 TEM images of Pd/ α -Al₂O₃ prepared by sonochemical method. Scale bar, 20 nm [18]



The synthesis in the presence of inorganic supports (such as silica and alumina) gives rise to highly active heterogeneous nanostructured catalysts [20, 55, 67, 68]. The precursors may be inorganic or organometallic.

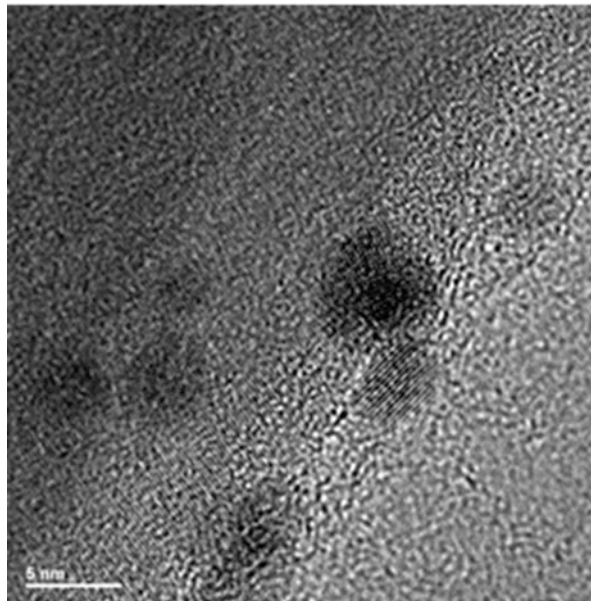
TEM images were obtained for the supported Pd/ α -Al₂O₃ catalyst (PdSON), as displayed in Figs. 13.14 and 13.15, showing clusters at the surface with mean size of 10 nm. Images with higher magnification, Fig. 13.15, show that these clusters are palladium crystallites with diameters less than 5 nm [18, 29].

Precipitation–Coprecipitation

To further investigate the aforementioned particle size effect, the aim is to develop a synthesis concept to obtain size-controlled Pd nanoparticles. In this approach, hydrotalcite-like compounds (HTlcs) are used as well-defined precursor materials, whose general formula is $[M_{2+1-x}M_{3+x}(\text{OH})_2](\text{An-})_x/n.m\text{H}_2\text{O}$ [2, 3]. In general, the flexibility of the choice of metal ions is quite high, and all cations in the range of 0.5–0.8 Å, such as $M^{2+} = \text{Mg}^{2+}, \text{Mn}^{2+}, \text{Co}^{2+}, \text{Ni}^{2+}, \text{Cu}^{2+}, \text{Zn}^{2+}$ and $M^{3+} = \text{Al}^{3+}, \text{Ga}^{3+}, \text{Fe}^{3+}, \text{Cr}^{3+}$, are capable of HTlc formation [69]. Divalent and trivalent metal cations are incorporated in brucite-like layers, and between these positively charged layers, charge-balancing anions, typically carbonate, maintain the electroneutrality of the lattice. Furthermore, the M^{2+}/M^{3+} ratio can be varied from approximately 0.2 to 0.4 to gain phase-pure materials.

Upon heating, HTlcs decompose into mixed oxides exhibiting high specific surface area, homogeneous metal distribution, and strong interaction between the individual elements. During reduction in H₂, noble metals such as Pd segregate out of the mixed-oxide matrix to form well-defined nanoparticles, whose size tends to depend on metal loading. PdMgAl hydroxycarbonates have already been studied by

Fig. 13.15 TEM images of higher magnification of the Pd/ α -Al₂O₃ prepared by sonochemical method. Scale bar, 5 nm [18]



several groups and were found to be active in phenol hydrogenation, oxidation of toluene, acetone condensation, hydrodechlorination of 1,2,4-trichlorobenzene, and total oxidation or coupling of methane [19, 25, 27].

The PdMgAl HTlc can be synthesized by controlled coprecipitation at pH = 8.5 and a temperature of 55 °C, by co-feeding appropriate amounts of mixed metal nitrate and sodium carbonate solutions. A sodium carbonate solution was used as precipitating agent. Both solutions were added simultaneously dropwise, as described elsewhere [19]. Transmission electron microscopy (TEM) images of Pd nanoparticles were acquired using a FEI TITAN microscope as displayed in Fig. 13.16.

After reductive treatment, the material has preserved the platelet-like morphology of the HTlc precursor, and small spherical particles were formed. HAADF-STEM micrographs were used to determine the particle size distribution. The good contrast between the metallic particles (white spots in Fig. 13.16b) and the MgO/MgAl₂O₄ support allowed for measuring of individual particles. It can be clearly seen that the particles are well dispersed and below 5 nm in size. Particles even smaller than 1 nm are also present. HRTEM images (Fig. 13.16c) show the presence of small Pd metal particles on the surface of the disordered oxide support. The average particle sizes of ≤ 3.5 nm are quite small considering the thermal treatment at 500 °C. Thus, some control over the particle size distribution of Pd is possible using the HTlc precursor approach for the preparation of supported Pd nanoparticles. The more the Pd²⁺ ions are diluted in the precursor lattice, the smaller the resulting Pd metal particles are after thermal reduction. These particles are thermally stable up to 500 °C and their size can be controlled to some extent

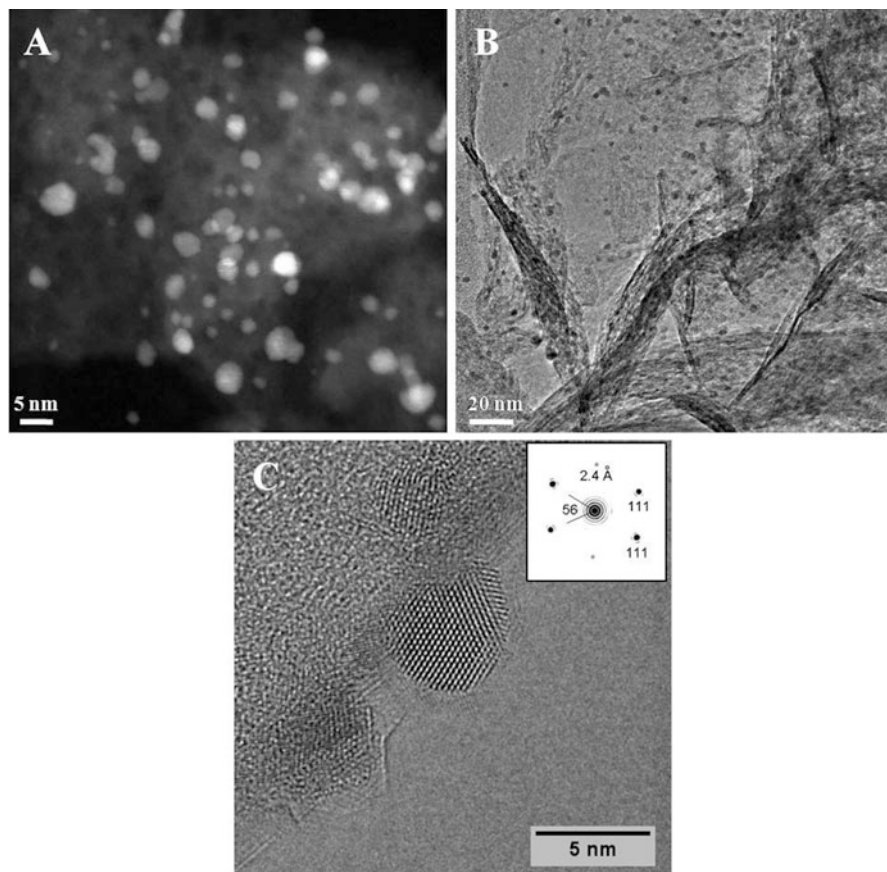


Fig. 13.16 (a) HAADF-STEM, (b) overview micrograph, (c) HRTEM of metallic Pd supported on MgO/MgAl₂O₄ (2.5 mol% *ex*-PdMgAl is shown) (Reproduced with permission from Moya et al., *Applied Catalysis A: General* 411–412 (2012) 105–113, 15)

between < 1.13 and 3.5 nm by adjusting the Pd content during synthesis (Fig. 13.17).

The sample with the lowest Pd loading of 0.33 wt% shows a much higher Pd dispersion compared to those samples with Pd contents between 1.5 and 8 wt%.

Activity Tests

In catalysis, there are also some examples of the dependence of activity and selectivity with the particle size and morphology of the active phase of the catalysts.

Iron catalysts supported on silica were synthesized by Suslick et al. [20]. The Fe / SiO₂ catalysts amorphous nature and particle size in the range 3–8 nm and were submitted to catalytic tests Fischer–Tropsch reactions, and their activities were compared with those of a catalyst Fe / SiO₂ prepared by dry impregnation of the

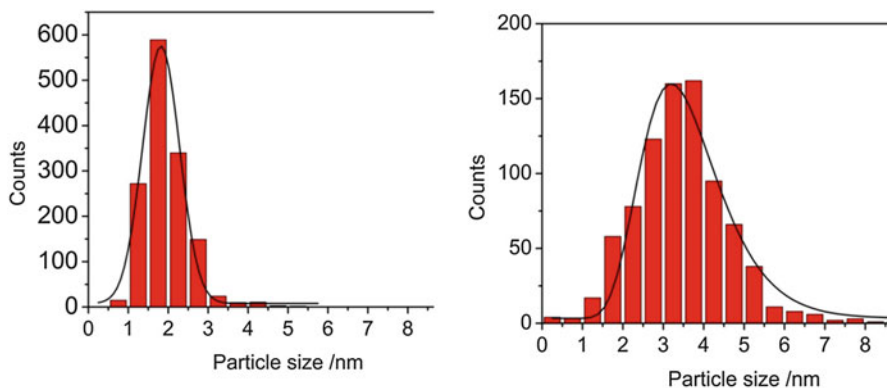


Fig. 13.17 Particle size distribution of Pd05 (a) and Pd25 (b) from TEM images [19]

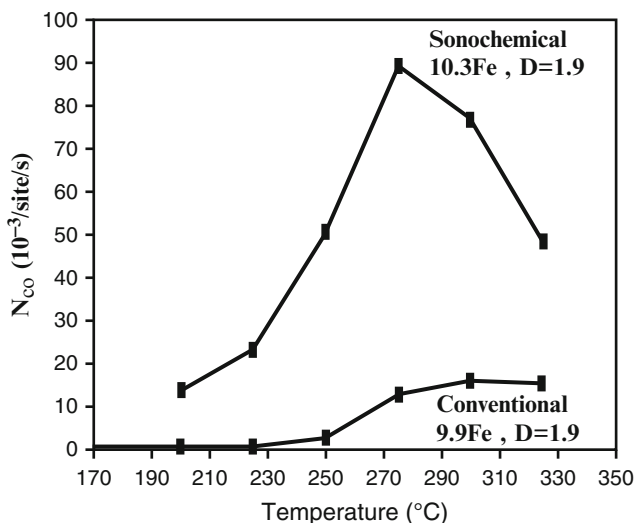


Fig. 13.18 Activity of Fe/SiO₂ for the Fischer–Tropsch reaction; sonochemical versus impregnation method preparation (Adapted with permission from Suslick et al., *Mater. Sci. Eng. A*, vol. 204 (1995) pp. 186–192)

same dispersion. The results of the activity as a function of temperature can be seen in Fig. 13.18.

El-Sayed and Narayanan [70, 71] observed that colloidal Pt catalysts have different rates for electron transfer reactions between ions and thiosulfate ferrocyanide. Kinetic studies were carried out, and the results were compared to the number of surface atoms in the vertices and edges of the nanocrystal structures for three different morphologies: cubic, tetrahedral, and spherical (the authors used the approach of cube–octahedral geometry for the calculation of the number of

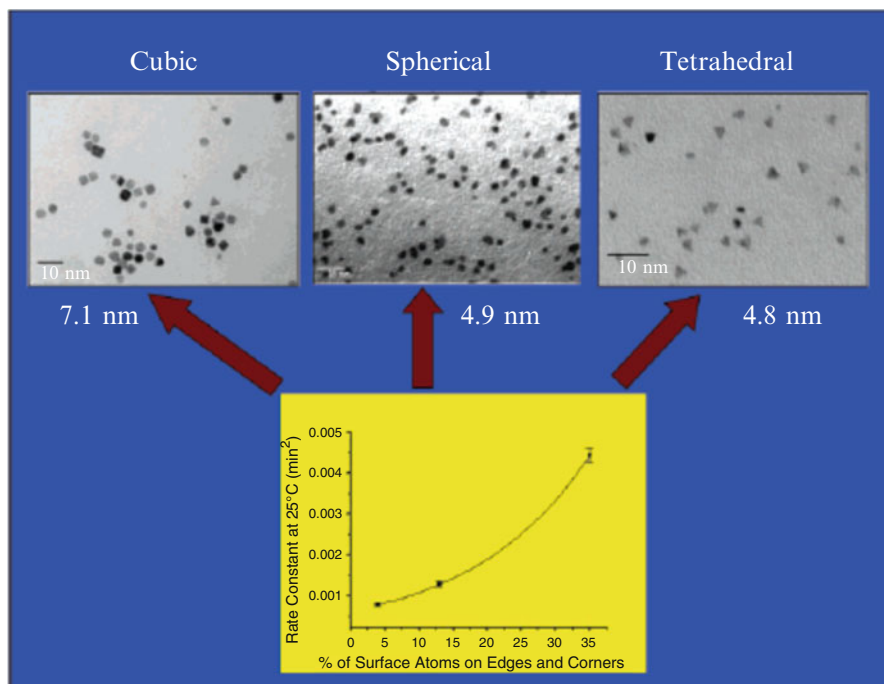


Fig. 13.19 Correlation of the catalytic activity with the fraction of surface atoms on surfaces and vertices (Narayanan, R., El-Sayed, M. A., *J. Phys. Chem. B*, vol. 109, 2005, 12663–12676, reproduced with permission)

sites, since these are, in fact, nearly spherical). The number of sites they occupy positions described interest can be obtained since characterized the exposed surfaces of the nanocrystals.

The plot of specific rate constant or activity versus percentage of surface tetrahedral atoms suggests that catalytic particles are the most active, followed by spherical and cubic, respectively (Fig. 13.19). This behavior shows a direct dependency of the activity to the amount of highly reactive sites. These results were corroborated with the determination of the reaction activation energy, which followed the order Pt tetrahedral $E_a < E_a$ spherical Pt $< E_a$ Pt Cubic.

13.1.5 Oxide Nanocrystals [18, 19, 24, 44, 51, 53, 63, 72–152]

Practices lead to the formation of nanocrystals with a wide range of sizes and shapes displaying a distribution of surface sites capable of promoting many different reactions. No molecular control on the nature of the active sites is expected, and only limited control on the selectivity of reactions can be achieved. Controlling the

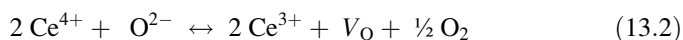
size of the nanocrystals used for catalysis can lead to huge changes in catalytic behavior. The importance of nanocrystallites and nanostructure to the performance of catalysts has stimulated wide efforts to develop methods for their synthesis and characterization, making this area of study an integral part of nanoscience [73]. Fortunately, metal nanoparticles can now be made with quite narrow size distributions by using, besides others, colloidal- [52] or dendrimer [53]-based chemistry. The morphology of these materials depends on the synthesis conditions and has been described by different authors as nanotowers, nanocone, nanobottle, nanoflowers, nanoarrows, nanorod, nanowires, and so on. The challenge is to disperse the colloidal nanoparticles on high surface area supports and to activate them without losing the original size and shape distribution. As a matter of fact, the control of the morphology of the nanoparticles, perhaps, seems to be more important than monitoring the performance of catalysts by controlling the size of the nanoparticles of the active phase. It has been known that some catalytic processes are structure sensitive, meaning that their activity or selectivity changes significantly with the method used for the catalyst preparation [73].

Cerium Oxide Nanocrystals

In the first example, we investigated the CeO_2 and CeO_2 -based materials. The higher performance of cerium oxide is assigned to the redox property ($\text{Ce}^{4+} \leftrightarrow \text{Ce}^{3+}$) promoting oxygen vacancies in the lattice, which are responsible for the high oxygen atom mobility. This is one of the important characteristics of ceria, allowing fluctuation between oxidant and reductant conditions due to the oxygen storage capability in the lattice structure [122]. However, Zhu and He [124] observed that pure CeO_2 is poorly thermostable and loses easily oxygen at high temperatures. Therefore, many authors added other metal ions or dopants to increase the stability and oxygen capability storage. The substitution of Ce^{4+} by dopants favored the reduction of the oxidation state of the Ce^{4+} to Ce^{3+} that maintains neutrality in the lattice and reduces the link stress bonding, depending on the dopant cation, which indeed favors the formation of new oxygen vacancies [115, 116, 125].

Different methods were used for the preparation of nanosized materials. CeO_2 is prepared by the precipitation and hydrothermal methods [126, 127]. The crystallite sizes are quite different depending of preparation methods [92]. These oxides present different oxidation states and evidence the presence of oxygen vacancies.

The EPR spectra are shown in Fig. 13.20 displaying signals between 3500 and 3600 Gauss attributed to the paramagnetic centers with axial symmetry $g \perp$ and $g \parallel$ associated to the Ce^{3+} cation (ion 4f1) with unpaired electrons [143, 144]. This signal is related to the Ce^{3+} cation. The intensity band may be associated to concentration of these species. Indeed, the oxygen vacancies are related to the reduction ability of the cation Ce^{4+} to Ce^{3+} , according to Adamski et al. [145], Wang et al. [146], and Appel et al. [147] as follows:



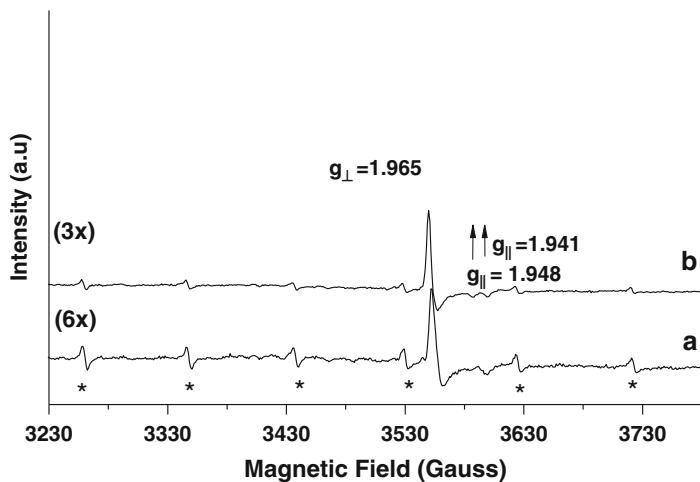
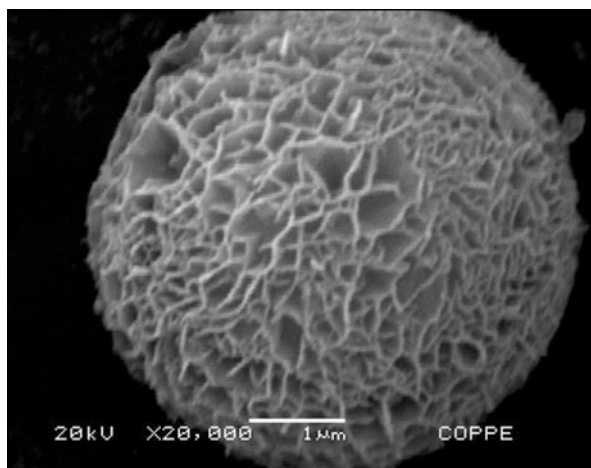


Fig. 13.20 EPR spectra of catalysts [115]

Fig. 13.21 SEM images of the CeO_2 (Flowerlike) [115]



where the ion O^{2-} is present in the lattice of ceria and V_{O} is the oxygen vacancy double charged with protons. This equation suggests that Ce^{3+} can be correlated to the concentration of the oxygen vacancies. Therefore, it also reveals strong defects in the crystalline lattice.

SEM observations displayed in Fig. 13.21 show that the CeO_2 flowerlike sample is nicely porous material with intercalated structured framework shapes.

Nickel Nanocrystals

In the second example, we prepared nickel nanocrystals with different morphologies which were synthesized by different methods:

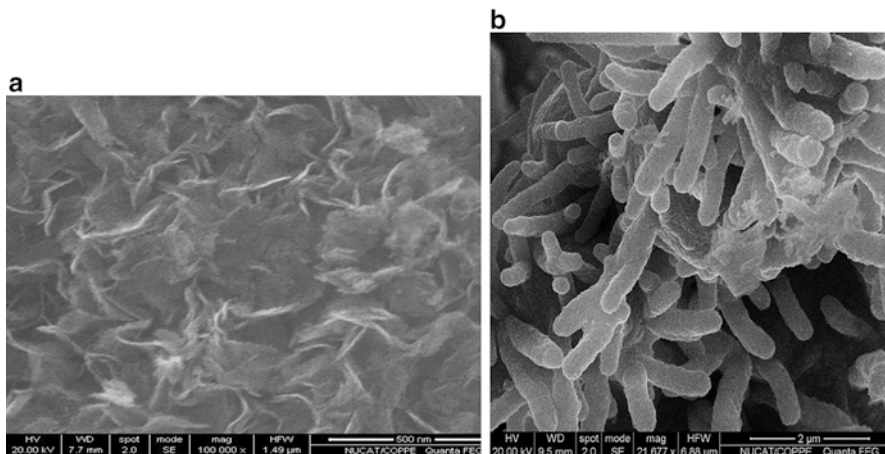


Fig. 13.22 SEM images of the NiEG sample (a) in oxide form: 100,000 \times ; SEM images of the NiDMG sample (b) in oxide form, 20,000 \times [73]

- Precipitation of nickel hydroxide with sodium carbonate precursor salts dissolved in ethylene glycol (NiEG), according to Li et al. [83]
- Precipitation of nickel dimethylglyoxime as precursor (NiDMG), according to Ni et al. [84].
- NiO was obtained after hydrotreatment and calcination of β -Ni(OH)₂ precursor (NiHT), according to Zhu et al. [85].

Figure 13.22 shows a nanoflower-like-type morphology in tridimensional form of NiO on the NiEG sample before the reaction. This morphology was originally observed on the hydroxide before calcination and seems to be very stable after thermal pretreatment; thus removing water did not damage the structure of the precursor. The structure did not collapse or fracture, which can be attributed to the excellent contact between nanoparticles with high orientation degree [83].

Figure 13.22b shows SEM images of NiO after calcination of the NiDMG precursor, indicating the presence of bidimensional rods, which suggests made up of small particles that gather forming rods. By removing the organic molecule (DMG) during heating, the arrangement of the structure of the precursor NiDMG was not affected, and according to [87], heating probably supplies energy to maintain the NiO nanoparticles highly oriented in the structure.

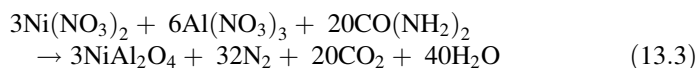
The Combustion Method

The combustion method has been proposed to synthesize nanosized crystallites and is particularly useful in the production of ultrafine ceramic powders with small average sizes. This is an easy and fast method, with the advantage of using inexpensive precursors, producing homogeneous nanosized crystallites, and highly reactive materials [101]. The combustion synthesis technique consists of the contact of a saturated aqueous solution of a desired metal salt and a suitable organic

fuel boiling until the mixture ignites and a self-sustaining and fast combustion reaction takes off, resulting in dry crystalline fine oxide powder (Patil [102, 103]). The large amount of gases released during the reaction produces a flame that can reach temperatures above 1000 °C. Kingsley et al. [105] described the preparation of aluminates with various metal nitrates (Mg, Ca, Sr, Ba, Mn, Co, Ni, Cu, and Zn) using urea or carbonylhydrazide as fuel. The fuel/oxidizer ratio was evaluated by Alinejad et al. [107] in the combustion synthesis of MgAl_2O_4 by using sucrose and PVA solution as fuels.

Nickel aluminate (NiAl_2O_4) is a good example of a mixed cation oxide with normal spinel structure, where Al occupies the octahedral sites and Ni occupies the tetrahedral sites [98, 113]. It can be used as support for catalysts due to its resistance to high temperatures and acidic or basic environments, providing chemical and physical stability for the catalyst.

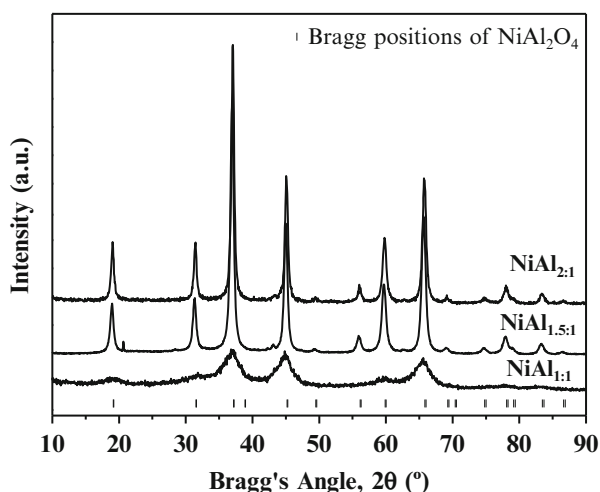
NiAl_2O_4 is prepared by the combustion method using urea as fuel. The stoichiometric ratio of urea to nitrate (U/N) needed to obtain NiAl_2O_4 powders is 2.2, assuming complete combustion, according to reaction 1 [94]:



The use of a stoichiometric U/N ratio resulted in a material with high surface area and homogeneous nanocrystallites, while the excess of fuel resulted in a nonporous material with low surface area.

X-ray diffractograms of the samples (Fig. 13.23) presented only a NiAl_2O_4 cubic spinel-type structure (JCPDS 10-0339). All samples showed mean crystallite nanosizes. The crystallite size is strongly dependent on the fuel/oxidant ratio, which increases with increasing urea loading. Nanosized crystallites of NiAl_2O_4

Fig. 13.23 XRD patterns of the samples NiAl (1:1), NiAl (1.5:1) and NiAl (2:1) [94]



were obtained by Han et al. [98, 113] applying the sonochemical method, but with very poor crystallinity.

The NiAl: (1:1) catalyst showed a high surface area ($186 \text{ m}^2/\text{g}$), similar to that reported in the literature, when using an expensive alkoxide precursor and a very long preparation time by the sol-gel method [96, 100, 111, 114]. The NiAl: (1:1) presented also unimodal pore size distribution in the range of 3–6 nm and pore volume of 0.18 mL/g , indicating mesoporous materials. On the contrary, the samples with excess of urea, NiAl: (2:1), presented lower surface area ($10 \text{ m}^2/\text{g}$) and nonporous material crystallite sizes of 13.2 and 16.6 nm, respectively. Nanosized crystallites of NiAl_2O_4 were obtained by Han et al. [98, 113] applying the sonochemical method, but with very poor crystallinity.

These results can be explained mainly through the flame temperature that was reached during the preparation. The combustion process with excess of urea caused a slower ignition of the reactant mixture, and the maximum temperature was much higher. The NiAl: (1:1) sample showed maximum peak at $1318 \text{ }^\circ\text{C}$ with an ignition time of 86 s, while the NiAl: (2:1) samples shifted the peaks to $1237 \text{ }^\circ\text{C}$ and ignition of 164 s. These results show that the excess of urea favors complete combustion during the synthesis, accompanied by the evolution of a large amount of gases, which contributes to the formation of materials with good crystallinity. However, agglomeration occurred at higher temperature, lowering the surface area, increasing average crystallite sizes and forming nonporous materials [94].

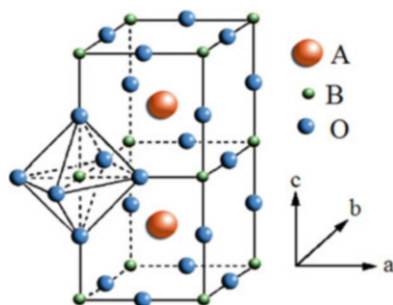
13.1.6 Mixed Oxides: Perovskite Structures Perovskites

The perovskite-type oxides have unique characteristics in response to a wide range of properties that are assigned to the cation substitution capacity in its structure, generating isostructural solid with formula $\text{A}_{1-x}\text{A}_x\text{B}_{1-y}\text{B}_y\text{O}_{3\pm\delta}$. These substitutions can lead to the stabilization of the structure with an unusual oxidation state for one of the cations and the creation of anionic and cationic vacancies. This has a significant influence on the catalytic activity of these materials compared to the typical supported materials. Another important feature is the thermal stability of these materials and mechanical and chemically stable reaction conditions [41, 148].

The ternary oxide of perovskite type can be divided into $\text{A}^{1+}\text{B}^{5+}\text{O}_3$, $\text{A}^{2+}\text{B}^{4+}\text{O}_3$, and $\text{A}^{3+}\text{B}^{3+}\text{O}_3$. The former is of particular interest because of their ferroelectric properties, e.g., KNbO_3 and NaNbO_3 e KTaO_3 ; $\text{A}^{2+}\text{B}^{4+}\text{O}_3$ probably forms the largest number of perovskite-type oxides, in which the cation may be an alkaline earth, cadmium, and lead, and B^{4+} includes Ce, Fe, Ti, Zr, Mo, and others. Finally, $\text{A}^{3+}\text{B}^{3+}\text{O}_3$ includes several compounds such as LaCrO_3 , EuFeO_3 , LaCoO_3 , etc. [153].

The ideal structure of a perovskite-type oxide is cubic, space group $Pm3m-O_h$, and A, a cation of large size coordinated to 12 oxygen ions, while B is a smaller cation coordinated to six oxygen ion. Schematically, Fig. 13.24 shows a unit cell

Fig. 13.24 Ideal structure of perovskite ABO_3 : the cation in the center of the unit cell; cation B in the center of an octahedron whose vertices are oxygen anions (Adapted from Fierro JLG, Peña MA. Chem Rev. 2001;101:1981–2018, [41])



ABO_3 , where the A cation occupies the center of the cube; cations are located at the vertices B, and oxygen anions are centered on the edges of the cube. Alternatively, the structure can be displayed with the B cation occupying the center of an octahedron formed of oxygen vertices, which in turn would be inside a cube whose vertices are the A cations.

For measuring the deviation from ideality of the cubic structure ABO_3 , Galasso [153] defined the tolerance factor t , according to Eq. (1). While in the ideal structure the atoms are in touch, this factor is calculated from the interatomic distances A_O and B_O , respectively, defined as $(r_A + r_O) = a/\sqrt{2}$ and $(r_B + r_O) = a/2$, which corresponds to cubic unit cell parameter.

$$t = \frac{(r_A + r_O)}{\sqrt{2}(r_B + r_O)} \quad (13.4)$$

The ideal cubic perovskite has a tolerance factor t equal to 1 and, only in some cases, approaches this factor at high temperatures. Most compounds present distortions, and the factor varies: $0.75 < t < 1.0$. However, when the tolerance factor is extrapolated beyond this range, the structure is no longer a perovskite and presents other structures, such as, limonite, calcite, and aragonite.

Besides the size of the ionic radii of A and B, there is another condition for the formation of a perovskite structure, which is electroneutrality; the sum of charge of cations must be equal to the sum of oxygen anion charge [41]. In heterogeneous catalysis, the most studied systems are those with an alkali element or alkaline earth lanthanide in position A, and a transition metal of the first set in position B (Ti, V, Cr, Mn, Fe, Co, Ni, Cu).

The structure of ABO_3 perovskite may also be modified by the partial substitution of the atoms of sites A and/or B, forming a new structure of $A_{(1-x)}A_xB_{(1-y)}B_yO_3$, in which x and y represent the degree of substitution. In general, the cation confers thermal and structural resistance, while B is responsible for the catalytic activity. However, the partial replacement of a cation can strongly affect the catalytic activity of B, due to the unusual stabilization oxidation state of this metal and due to the simultaneous formation of structural defects.

In addition, the partial substitution of the cation B can modify the catalytic activity that interferes directly the electronic state of d-orbital, the stabilization energy of the crystal field and the B–O binding energy [154]. The partial substitution represents, therefore, a fundamental tool for obtaining active, selective, and stable materials for various applications.

The nonstoichiometry, which indicates the cation deficiency in the sites A and/or B, as well as of oxygen, is a very common feature of perovskites, different from the ideal structure. In the case of oxygen site, nonstoichiometry obtained by the presence of vacancy is more common than that generated by the cationic vacancies. Therefore, the most common nonstoichiometric structures are those with a relative excess of cations due to anionic vacancies. On the other hand, the excess of oxygen is not common, probably because the extra oxygen introduced in the network is thermodynamically unfavorable.

The presence of vacancies and defects in the structure of the catalyst is largely responsible for the mobility of oxygen within the crystal lattice; the more vacancies, the greater the mobility of oxygen. The ion vacancies affect the catalytic activity to promote or not the adsorption of gas phase reactants [155].

Synthesis of Mixed Oxides Perovskite Type

The synthesis of oxide perovskite type requires a methodology that provides a homogeneous solid, maximizing the specific area. The properties of these systems, such as texture, oxidation state of the cation, stoichiometry, and structure, depend on the synthesis method. For this reason, the literature has reported a series of preparation methods, and in particular the methodologies known as sol–gel have shown promising results allowing excellent control over the properties of the synthesized perovskites.

The sol–gel technique is one of the most popular processes for powder synthesis, films, fibers, monoliths, and other materials used in engineering. It basically involves the formation of an inorganic and/or organic network via a chemical reaction in solution, generally at low temperature, followed by the transition from solution to a *colloidal sol* and a *multigel*. According to the different precursors employed, the sol–gel techniques are classified as follows:

1. Sol–gel route based on the hydrolysis–condensation of metal alkoxides
2. Chelate gel route, which is the concentration of aqueous solutions and involving chelated metals
3. Polymerizable compound route (PCR) based on the use of metal salts such as precursors, citric acid, and ethylene glycol as a chelating agent such as polyesterification

The latter route is also known as the Pechini method and has been used to prepare multicomponent metal oxides with a high homogeneity [43]. In short, the route of the polymerizable compound (PCR) process combines the formation of metal complexes and organic in situ *polymerization*. The schematic representation of this process is illustrated in Fig. 13.25.

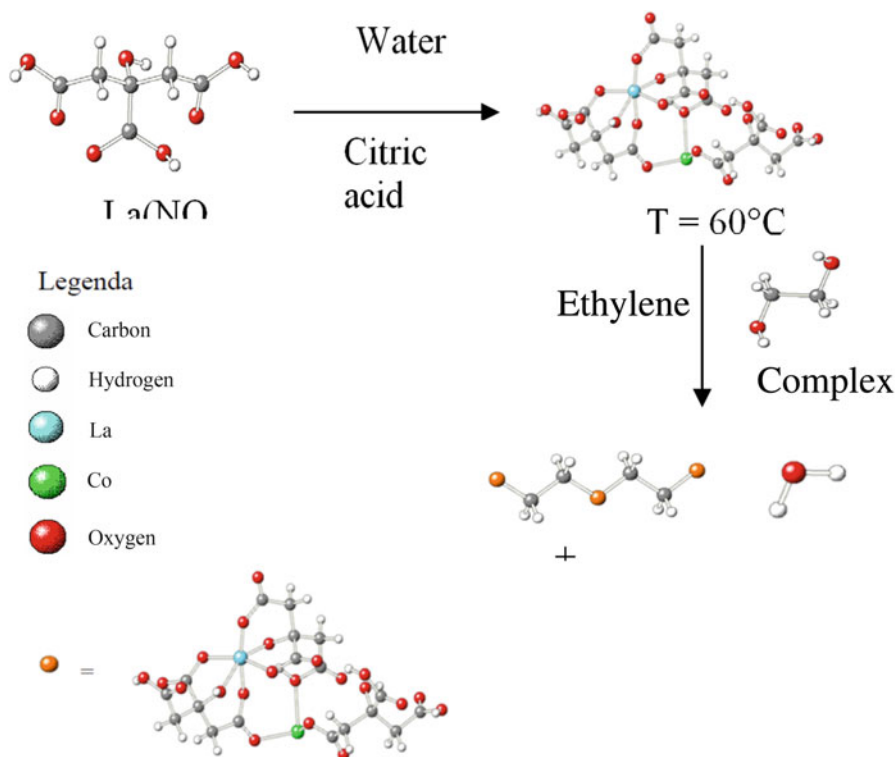


Fig. 13.25 Synthesis of LaCoO_3 perovskite: Pechini (Adapted from [156])

Usually an α -hydroxy-carboxylic acid, e.g., citric acid, is used to form chelates with the metal cations from the salt precursor. In the presence of a polyhydroxy alcohol, e.g., ethylene glycol, these chelates react with the alcohol to form ester and water as products. When the mixture is heated a polyesterification occurs in the liquid solution creating a homogeneous *colloidal solution* (sol), in which ions are uniformly distributed in the organic polymer matrix. Upon removal of the solvent, an intermediate resin is formed. Finally, the oxide structure is obtained by removal of organic substances by means of calcination [157].

The resin produced by PCR contains a large amount of organic material that must be totally eliminated for obtaining the perovskite. In this sense, the thermogravimetric analysis is performed in order to identify the sample decomposition temperature and thus can be properly infer the calcination temperature of the polymeric precursor.

Popa et al. [158] compared the synthesis of the perovskite LaCoO_3 by PCR with the *non-polymerizable* route, using citric acid as a complexing agent, without the use of ethylene glycol (also known as the amorphous citrate method). According to the X-ray diffraction results, the materials prepared by the amorphous citrate method showed some minor unidentified diffraction peaks, in addition to LaCoO_3 ,

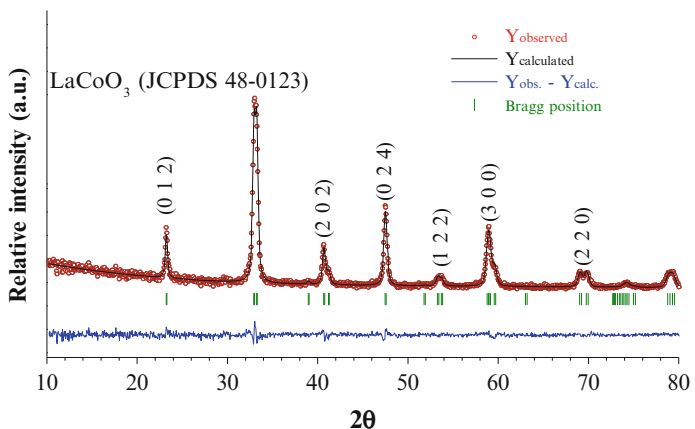


Fig. 13.26 Diffractogram of LaCoO₃ perovskite (JCPDS48-0123) [44]

phase for samples calcined at $T = 600, 650$ and 700 °C. Moreover, catalyst synthesized by PCR appeared pure perovskite phase after calcination even at $T = 1300$ °C.

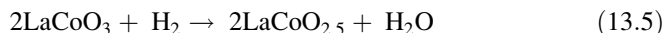
The XRD pattern of the calcined perovskite mass at 700 °C is shown in Fig. 13.26. The peaks relating to the main crystallographic planes are identified with their Miller indices [44].

The crystallographic parameters were used in the calculation of the average crystallite size resulting in 24.2 nm.

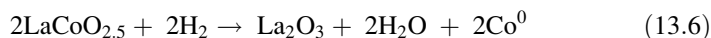
The active phase of the catalyst is obtained after the reduction of LaCoO₃ precursor. The appropriate reduction allows obtaining metallic cobalt catalyst (Co) dispersed in a matrix oxide La₂O₃, which confers structural stability to the material [159].

The reducibility of the perovskite LaCoO₃ is performed by temperature-programmed reduction and allows investigating the reduction degree. The TPR profile of this sample is shown in Fig. 13.27 and presents two reduction peaks at around 270 – 490 °C and 500 – 700 °C, respectively.

According to Villoria et al. (2011), the peak at lower temperature, centered at 426 °C, is attributed to the reduction of Co³⁺ to Co²⁺ perovskite structure, forming the structure brownmillerite LaCoO_{2.5}:



The second peak, centered at higher temperatures, corresponds to the reduction of Co²⁺ to Co⁰.



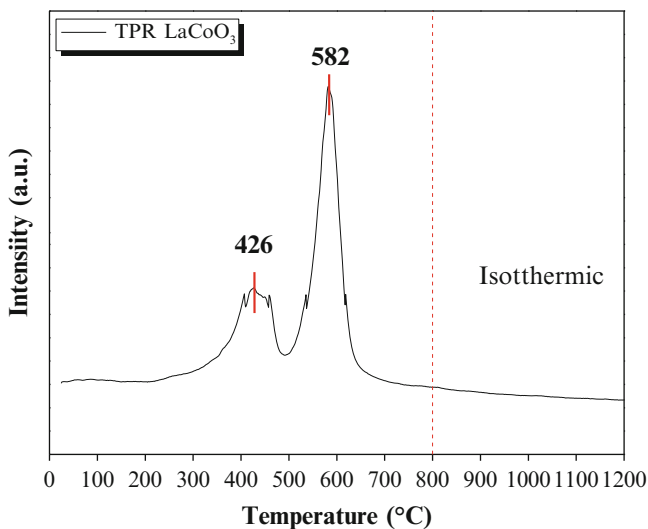


Fig. 13.27 Reducibility of the perovskite LaCoO₃ [37]

13.2 Part II: Graphenes

Graphenes are two-dimensional one-atom-thick planar sheet of sp^2 -bonded carbon atoms, having a thickness of 0.34 nm, and are well known for electronic, mechanical, optical, thermal, and catalytic systems [5]. It has been used in the development of novel nanomaterials in various applications, such as electronic devices [4, 5, 160–162], nanoelectronics [163], composites [164], electron microscopy substrate materials [165], and catalysis [166]. While these applications have attracted attention of scientists in the nanomaterial area, the realization of potential applications is limited by difficulties in mass production of graphene.

Graphene research has expanded quickly. Andre Geim and Konstantin Novoselov at the University of Manchester won the Nobel Prize in Physics in 2010 “for groundbreaking experiments regarding the two-dimensional material graphene” [4].

Definition: The recent definition of graphene can be given as a two-dimensional monolayer of carbon atoms, which is the basic building block of graphitic materials (i.e., fullerene, nanotube, graphite) [165].

13.2.1 Syntheses of Graphenes

1. *Exfoliation and cleavage:* The mechanical exfoliation is a peeling process generating thin flakes, which are composed of monolayers or few layers of graphene. Chemical oxidation and subsequent exfoliation generate oxide

monolayers and structural defects. However, reduction or thermal treatment is impossible to regenerate graphene. Blake et al. and Hernandez et al. have demonstrated that graphite could be exfoliated in *N*-methyl-pyrrolidone to produce defect-free monolayer graphene [167, 168]. The disadvantage of this process is the high cost of the solvent and the high boiling point of the solvent.

2. *Chemical vapor deposition (CVD)*: In 2006, Novoselov and coworkers synthesized few layers of graphene films by CVD, using camphor as the precursor on Ni foils [169]. This study opened up a new graphene synthesis route. The growth mechanism of graphene on substrates mediates high carbon solubility (>0.1 atomic %) such as Co and Ni [170, 171]. The thickness of the precipitated carbon (graphene layers) is controlled by the cooling rate.
3. *Chemical process route*: This is the most important route to produce graphene for several applications in catalysis and materials, in particular for hydrogen storage in fuel cells and Fischer–Tropsch, recently. Three principal methods are developed by Brodie [172], Staudenmaier [173], and Hummers and Offeman [174], respectively.

Graphite oxide (GO) is usually synthesized through the oxidation of graphite using oxidants including concentrated sulfuric acid, nitric acid, and potassium permanganate based on Hummers method [175]. GO is highly hydrophilic and readily exfoliated in water, yielding stable dispersion consisting mostly of single-layered sheets (graphene oxide). Graphene oxide is a monolayer material produced by the exfoliation of GO. When prepared by sonication, they form homogeneous and stable sheets with uniform thickness. Exfoliation of GO was also attained for *N*, *N*-dimethylformamide (DMF), tetrahydrofuran (THF), *N*-methyl-2-pyrrolidone (NMP), and ethylene glycol [176]. Li et al. showed that the surface charges are highly negative [177]. In fact, the formation of stable graphene oxide was attributed to not only its hydrophilicity but also the electrostatic repulsion.

GO can be reduced to graphene sheets (GNS) by NaBH_4 [174], hydroquinone [174] and hydrogen sulfide [167]. Stankovich et al. [168] investigated the chemical reduction of exfoliated graphene oxide sheets with several reducing agents and found hydrazine hydrate ($\text{H}_2\text{NNH}_2 \cdot \text{H}_2\text{O}$) to be the best one in producing very thin graphene-like sheets. Surface area measurement of the reduced GO sheets is in the order of $460 \text{ m}^2 \text{ g}^{-1}$. However, it is still lower than the theoretical specific surface area for completely exfoliated and isolated graphene sheets []. According to Saner et al. [178], the best method for the production of mostly exfoliated (minimum number of layers) graphene nanosheets is the oxidation of the sonicated graphite flake, ultrasonic treatment of GO, and chemical reduction of sonicated GO samples (Antolini [5]).

The functionalization of graphene oxide is important for various applications. There are two approaches: covalent functionalization and non-covalent functionalization.

Functionalized GNS by surface epoxy, hydroxyl, and carboxyl groups are synthesized through simple synthesis processes. These processes include the chemical oxidation of common graphite to graphite oxide and the subsequent thermal exfoliation of the GO to GNS [165, 179]. Figure 13.28 shows an illustration of the synthetic route used to obtain the GNSs and their SEM images [180].

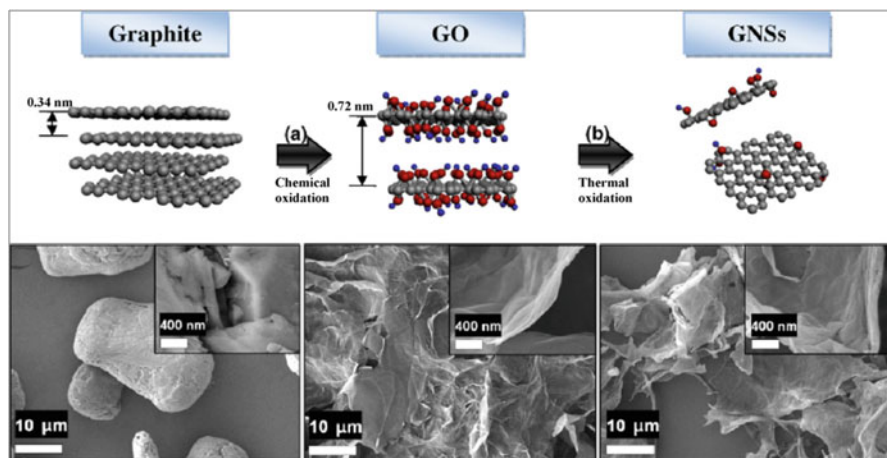


Fig. 13.28 The SEM image of graphite shows a *bulky* and *spherical* shape. After the chemical oxidation and thermal exfoliation (S.M. Choi, M.H. Seo, H.J. Kim, W.B. Kim, Carbon 49 (2011) 904–909, reproduced with permission from Elsevier) [167]

McAllister et al. [181, 181a] presented a detailed analysis of the thermal expansion mechanism of graphite oxide to produce functionalized graphene sheets.

The non-covalent functionalization of graphene oxide utilizes the weak interactions between the graphene oxide and target molecules. The network on graphene oxide provides interactions with conjugated polymers and aromatic compounds that can stabilize reduced graphene oxide resulting from chemical reduction and produce functional composite materials.

Results showed that GO reduced to few-layer level has poor dispersion in water. Zhang et al. (2004) showed an alternative method for removing epoxy and hydroxyl groups from GO with a sodium acetate trihydrate [182]. This approach may open up the new possibility for cost-effective, environment-friendly, and large-scale production of graphene. They proposed a one-step reduction of GO and demonstrated an easy efficient route to prepare graphene, employing sodium acetate trihydrate as a reducing agent.

GO was prepared from graphite powder through the modified Hummers method [183]. Graphene was synthesized via the chemical reduction of GO by sodium acetate trihydrate. A typical procedure was 1.10 g $\text{CH}_3\text{COONa}\cdot 3\text{H}_2\text{O}$ dispersed into 55 mL of GO dispersion (1 mg/mL).

13.2.2 Syntheses of Metals on Graphene Nanosheets

There are two ways to prepare Me/GNS, that is, (1) simultaneous and (2) sequential reduction of GO and metal precursors. Metal precursors are deposited on GO and then are reduced simultaneously by different methods such as ethylene glycol, [164, 169, 170, 177, 182, 184, 185], NaBH_4 [186, 187], PVP/hydrazine [171],

sodium citrate [188, 189] microwave heating [190], microwave polyol [191–194], and colloidal methods [195].

Pt/GNS was prepared by reduction of H_2PtCl_6 and GO suspension using NaBH_4 [187], as discussed before. It is difficult to prepare directly. Thus, the sequential method is overall used to prepare catalysts supported on functionalized graphene. There are two possibilities: electrochemical reduction of GO, followed by the electrochemical deposition and reduction of Pt precursor [196], and (2) in the photocatalytic reduction of GO, followed by the injection of Ag, Au, and Pd precursors on the graphene surface [197, 198].

13.2.3 Structure

The structural characteristics of GNS and Pt/GNS are shown in Figs. 13.29 and 13.30 [177, 199].

XRD analysis showed a diffraction peak of GO at $2\theta = 11.2^\circ$ (002) which is consistent with interlayer space (d-spacing) of 0.7130 nm. This value is larger than the d-spacing (0.335 nm) of pristine graphite ($2\theta = 26.7^\circ$), as a result of the intercalation of water molecules and the formation of oxygen-containing functional groups between the layers of graphite during oxidation [200]. For RGO, the 002 reflection peak at $2\theta = 11.2^\circ$ disappeared and a weak and broad diffraction peak at $2\theta = 25.4^\circ$ appeared, consistent with d-spacing of 0.350 nm, suggesting the graphene network. This proves the formation of few layers of graphene.

Typical FETEM image of the as-synthesized RGO is shown in Fig. 13.30.

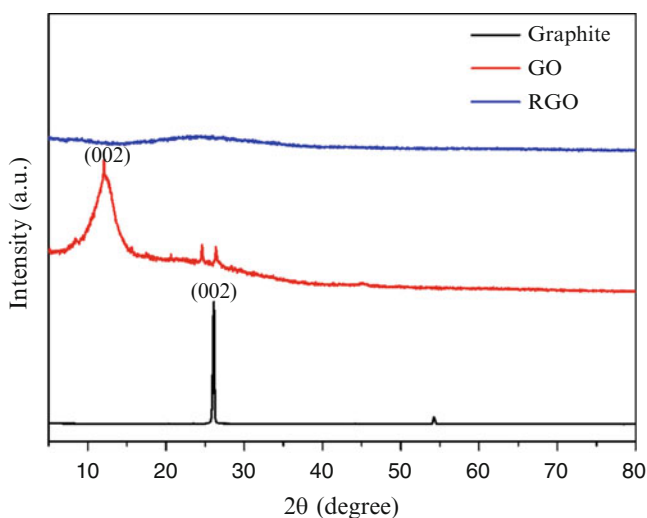


Fig. 13.29 XRD patterns of pristine graphite, GO, and RGO (Reproduced with permission from Zhang et al., *Synthetic Metals* 193 (2014) 132–138) [215a]

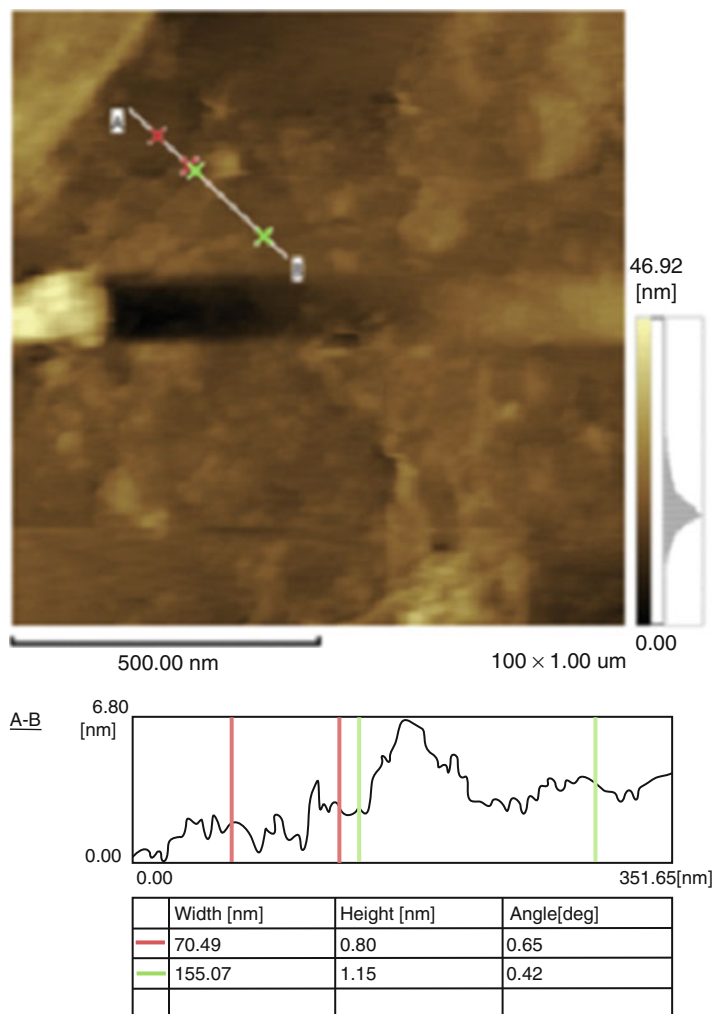


Fig. 13.30 Typical FETEM image of the as-synthesized RGO at different magnifications (X. Zhang et al., *Synthetic Metals* 193 (2014) 132–138, reproduced with permission) [215a]

Raman spectroscopy of GO is shown in Fig. 13.31 and indicates D, G, and 2D peaks around 1350 cm^{-1} , 1580 cm^{-1} , and 2700 cm^{-1} , which allows characterization of graphene layers in terms of number of layers present. The D band appears due to the presence of disorder in atomic arrangement or edge effect of graphene, ripples, and charge puddles. Comparison of Raman spectra between graphite and single- and few-layer graphene is shown in Fig. 13.30 [191]. There is a significant change in shape and intensity for 2D band of , graphene and graphite.

Figure 13.32 shows the XRD pattern of Pt/GNS, evidencing the disappearance of the graphite peak at 2θ about 26.4° and the appearance of a peak at 2θ at 10.4° ,

Fig. 13.31 Comparison of Raman spectra at 513 nm for the graphite and single-layer graphene (Reproduced with permission from Zhang et al., *Synthetic Metals* 193 (2014) 132–138) [215a]

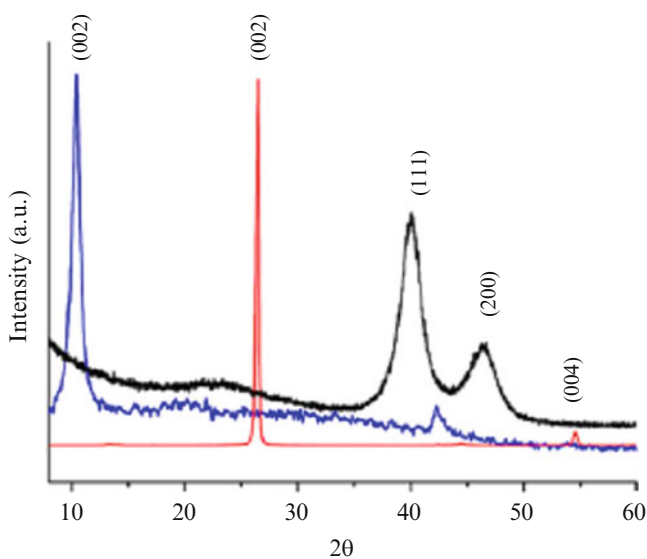
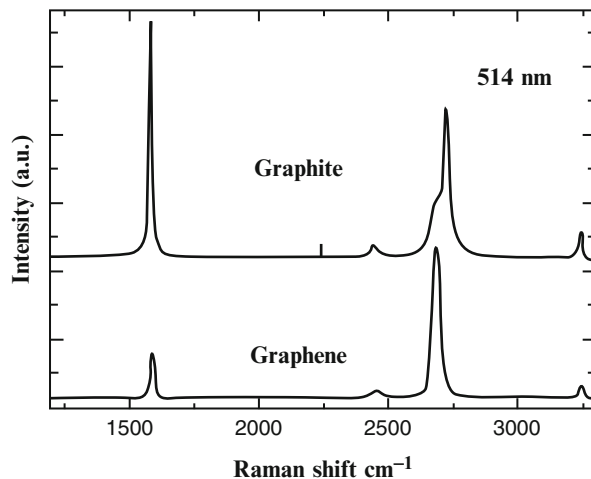


Fig. 13.32 XRD patterns of graphite (red line, bottom), graphite oxide (blue line, middle) and Pt/graphene (black line, top). Reproduced with permission from Y. Li, L. Tang, J. Li, *Electrochemistry Communications* 11 (2009) 846–849 [160]

revealing the successful oxidation of the starting graphite (C). The diffraction peaks at $2\theta = 31.3^\circ$ and 46.2° correspond to the (1 1 1), and (2 0 0) facets of platinum crystals. As shown, GO was fully exfoliated into nanosheets with micrometer-long wrinkles by ultrasonic treatment, illustrating clearly the flake-like shapes of graphite oxide sheets.

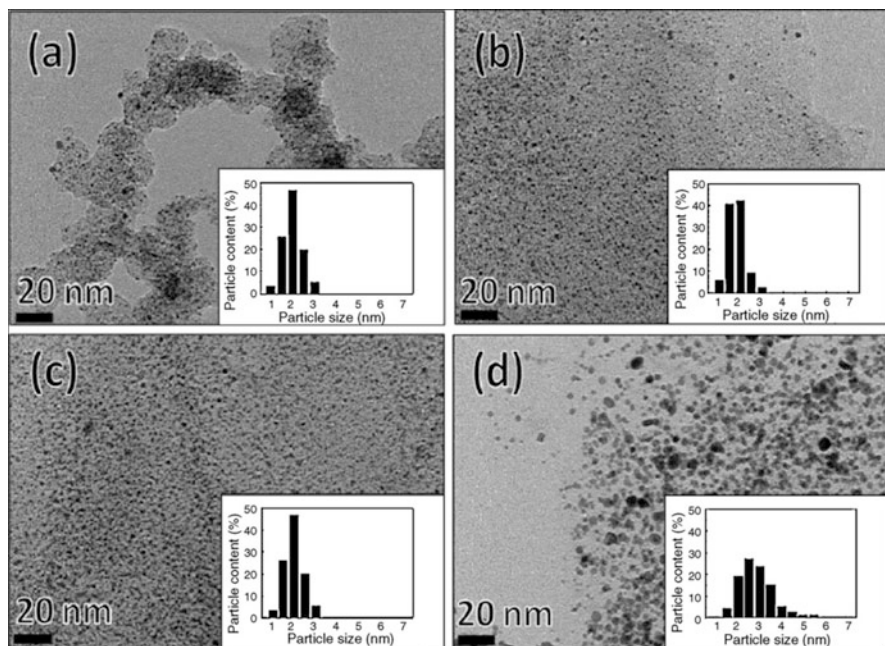


Fig. 13.33 TEM images of the (a) 40 wt% Pt/C, (b) 40 wt%, (c) 60 wt%, and (d) 80 wt% Pt/GNS catalysts (S.M. Choi, M.H. Seo, H.J. Kim, W.B. Kim, Carbon 49 (2011) 904–909, reproduced with permission) [167]

TEM images of the Pt/f-GNS catalysts revealed that for the Pt/f-GNS catalyst the Pt nanoparticles were highly dispersed even up to 80 wt% Pt/f-GNS, as shown in Fig. 13.33.

13.3 Conclusion

The literature [201–257] presents new catalysts of metallic or oxides supported on NCT and in particular on graphenes for several applications, such as hydrogen production for fuel cells and metals supported on graphenes for the Fisher–Tropsch synthesis. However, compared to the number of paper on catalytic processes, few works have been reported and tested with graphene-supported catalysts. In fact, the combination of the high surface area, high conductivity, unique graphitized basal plane structure, and potential low manufacturing cost makes graphene sheets a promising candidate as catalyst. Additional references related to this subject [201–257].

References

1. Aiken III JD, Finke RG. *J Mol Catal A*. 1999;135:1–44.
2. Burda C, Chen X, Narayanan R, El-Sayed MA. *Chem Rev*. 2005;105:1025–102.
3. Narayanan R, El-Sayed MA. *Nano Lett*. 2004;4:1343–8.
4. Wikipedia: the free encyclopedia.htm. file:///D:/Carbon%20nanotube%20
5. Antolini E. *Appl Catal Environ*. 2012;123–124:52–68.
6. Roucoux A, Schulz J, Patin H. *Chem Rev*. 2002;102:3757–78.
7. Moulijn JA, van Leeuwen PWN, van Santen RA. *Catalysis*. In: Geus et al, editors. *Studies in surface science and catalysis*, Chap. 9; 1995, vol. 79, p. 339.
8. Wang X, Zhuang J, Peng Q, Li Y. *Nature*. 2005;437:121–4.
9. Cushing BL, Kolesnichenko VL, O'Connor CJ. *Chem Rev*. 2004;104:3893–946.
10. Weare WW, Reed SM, Warner MG, Hutchinson JE. Improved synthesis of small phosphine-stabilized gold nanoparticles. *J Amer Chem Soc*. 2000;122:12890–1.
11. Yao H, Momozawa O, Hamatami T, Kimura K. Stepwise size selective extraction of carboxylate-modified gold nanoparticles from an aqueous suspension into toluene with trioctylammonium cations. *Chem Mater*. 2001;13:4692–7.
12. Okitsu K, Mizukoshi Y, Bandow H, Maeda Y, Yamamoto T, Nagata Y. Formation of the noble metal nanoparticles by ultrasonic irradiation. *Ultrason Sonochem*. 1996;3:S249–51.
13. Okitsu K, Bandow H, Maeda Y. Sonochemical preparation of ultrafine palladium nanoparticles. *Chem Mater*. 1996;8:315–7.
14. Leff DV, Brandt L, Heath JR. Synthesis and characterization of hydrophobic organically soluble gold nanocrystals functionalized with primary amines. *Langmuir*. 1996;12:4723–30.
15. Teranishi T, Miyake M. Size control of palladium nanoparticles and their crystal structures. *Chem Mater*. 1998;10:594–600.
16. El-Sayed MA. *Acc Chem Res*. 2001;34:257–64.
17. Toniolo FS, Moya S, Schmal M. *Adv Chem Lett*. 2013;1:1–8.
18. Moya SF, Martins RL, Ota A, Kunkes EL, Behrens M, Schmal M. *Appl Catal Gen*. 2012;411–412:105–13.
19. Ota A, Kunkes EL, Kröhnert J, Schmal M, Behrens M. *Appl Catal Gen*. 2013;452:203–13.
20. Suslick KS, Hyeon T, Fang M, Cichowlas AA. *Mater Sci Eng A*. 1995;204:186–92.
21. Narayanan R, El-Sayed MA. *J Phys Chem B*. 2005;109:12663–76.
22. Lee MB, Yang QY, Ceyer ST. *J Chem Phys*. 1987;87:2724–41.
23. Valden M, Pere J, Xiang N, Pessa M. *Chem Phys Lett*. 1996;257:289–96.
24. Beebe Jr TP, Goodman DW, Kay BD, Yates JT. Kinetics of the activated dissociative adsorption of methane on the low index planes of Ni single crystal surfaces. *J Am Chem Soc*. 1987;87:2305–15.
25. Choudhary TV, Goodman DW. *Top Catal*. 2002;20:35–42.
26. Goodman DW. *J Phys Chem*. 1996;100:13090–102.
27. In YZ, Sun J, Yi J, Lin JD, Chen HB, Liao DW. *J Mol Struct Theochem*. 2002;587:63–71.
28. Ciobica IM, Van Santen RA. *J Phys Chem B*. 2002;106:6200–5.
29. Moya SF. tese de doutorado. COPPE, Universidade Federal do Rio de Janeiro, Rio de Janeiro, RJ; 2008.
30. Teranishi T, Miyake M. *Chem Mat*. 1999;10:594–600.
31. Thompson LH, Doraiswamy LK. *Ind Eng Chem Res*. 1999;38:1215–49.
32. Oh H-S, Yang KJ, Costello CK, Wang YM, Bare SR, Hung HH, Kung MC. *J Catal*. 2002;210:375–86.
33. Lee S-J, Gavriilidis A. *J Catal*. 2002;206:305–13.
34. Haruta M. *J New Mater Electrochem Syst*. 2004;7:163–72.
35. Wolf A, Schüth F. *Appl Catal A*. 2002;226:1–13.
36. Ribeiro NFP, Mendes FMT, Perez CAC, Souza MMVM, Schmal M. *Appl Catal A*. 2009;347:62–71.
37. Turkevich J, Stevenson PC, Killier J. *Disc Faraday Soc*. 1951;11:55.

38. Turkevich J. *Gold Bull.* 1985;18:86.
39. Duff DG, Baiker A, Edwards PP. *Langmuir.* 1993;9:2301–9.
40. Duff DG, Baiker A, Gameson I, Edwards PP. *Langmuir.* 1993;9:2310–7.
41. Fierro JLG, Peña MA. *Chem Rev.* 2001;101:1981–2018.
42. Tejuca LG, Fierro JLG, Tascon JMD. *Adv Catal.* 1989;36:237–328.
43. Lin J, Yu M, Lin C, Liu X. *J Phys Chem C.* 2007;111:5835.
44. Magalhães RNSH, Toniolo FS, da Silva VT, Schmal M. *Appl Catal A Gen.* 2010;388:216–24.
45. Ko E-Y, Park ED, Seo KW, Lee HC, Lee D, Kim S. *Catal Today.* 2006;116:377.
46. Bialobok B, Trawczynski J, MisTa W, Zawadzki M. *Appl Catal B.* 2007;72:395.
47. Oliva C, Cappelli S, Kryukov A, Chiarello GL, Vishniakov AV, Forni L. *J Mol Catal A Chem.* 2006;255:36.
48. Wen Y, Zhang C, He H, Yu Y, Teraoka Y. *Catal Today.* 2007;126:400–5.
49. Forni L, Oliva C, Vatti FP, Kandala MA, Ezerets AM, Vishniakov AV. *Appl Catal B.* 1996;7:269–84.
50. French SA, Catlow CRA, Oldman RJ, Rogers SC, Axon SA. *Chem Commun.* 2002;22:2706–7.
51. Viswanathan B, George S. *React Kinet Catal Lett.* 1985;27:321–4.
52. Shannon RD. *Acta Crystallogr A.* 1976;32:751.
53. Hadjiev I, Iliiev MN, Vergilovs IV. *J Phys C Solid State Phys.* 1988;21:L199–201.
54. Wang ZL, Petroski JM, Green TC, El-Sayed MA. *J Phys Chem B.* 1999;102:6135–51.
55. Okitsu K, Yue A, Tanabe S, Matsumoto H. *Chem Mater.* 2000;12:3006–11.
56. Miyazaki A, Balint I, Nakano Y. *J Nanop Res.* 2003;5:69–80.
57. Duteil A, Schmid G, Meyer-Zaika W. *J Chem Soc Chem Commun.* 1995;31–32.
58. Kumar RV, Diamant Y, Gedanken A. Sonochemical synthesis and characterization of nanometer-size transition metal oxides form metal acetates. *Chem Mater.* 2000;12:2301–5.
59. Liang J, Jiang X, Liu G, Deng Z, Zhuang J, Li F, Li Y. Characterization and synthesis of pure ZrO₂ nanopowders via sonochemical methods. *Mater Res Bull.* 2003;38:161–8.
60. Srivastava DN, Perkas N, Zaban A, Gedanken A. Sonochemistry as a tool for preparation of porous metal oxides. *Pure Appl Chem.* 2002;74:1509–17.
61. Mizukoshi Y, Takagi E, Okuno H, Oshima R, Maeda Y, Nagata Y. Preparation of platinum nanoparticles by sonochemical reduction of the Pt(IV) ions: role of surfactants. *Ultrason Sonochem.* 2001;8:1–6.
62. Hyeon T, Fang M, Suslick KS. Nanostructure molybdenum carbide: sonochemical synthesis and catalytic properties. *J Amer Chem Soc.* 1996;118:5492–3.
63. Liu BS, Au CT. *Appl Catal A.* 2003;244:181–95.
64. Zhu J, Aruna ST, Kolytyn Y, Gedanken A. A novel method for the preparation of lead selenide: pulse sonoelectrochemical synthesis of lead selenide nanoparticles. *Chem Mater.* 2000;12:143–7.
65. Qiu L, Wei Y, Pol VG, Gedanken A. Synthesis of a-MoTe₂ nanorods via annealing Te-seeded amorphous MoTe₂ nanoparticles. *Inorg Chem.* 2004;43:6061–6.
66. Thompson LH, Doraiswamy LK. Sonochemistry : science and engineering. *Ind Eng Chem Res.* 1999;38:1215–49.
67. Li H, Wang R, Hong Q, Chen L, Zhong Z, Kolytyn Y, Calderon-Moreno J, Gedanken A. Ultrasound assisted polyol method for the preparation of SBA-15 supported ruthenium nanoparticles and the study of their catalytic activity on the partial oxidation of methane. *Langmuir.* 2004;20:8352–6.
68. Dhas NA, Ekhtiarzadeh A, Suslick KS. Sonochemical preparation of supported hydrodesulfurization catalysts. *J Amer Chem Soc.* 2001;123:8310–6.
69. Yang QY, Johnson AD, Maynard KJ, Ceyer ST. Synthesis of benzene from methane over a Ni(111) catalyst. *J Am Chem Soc.* 1989;111:8748–9.
70. Narayanan R, El-Sayed MA. Shape-dependent catalytic activity of platinum nanoparticles in colloidal solutions. *Nano Lett.* 2004;4:1343–8.

71. Narayanan R, El-Sayed MA. Changing catalytic activity during colloidal platinum nanocrystals due to the shape changes: electron transfer reactions. *J Amer Chem Soc.* 2004;126:7194–5.
72. Orlovskaya N, Steinmetz D, Yarmolenko S, PAI D, Sankar J, Goodenough J. *Phys Rev B.* 2005;72:220.
73. Martins RL, Schmal M. *J Braz Chem Soc.* 2013;25(12):2399–408.
74. Martins RL, Baldanza MAS, Souza MMVM, Schmal M. *Appl Catal A Gen.* 2007;318:207.
75. Moya SF, Martins RL, Schmal M. *Appl Catal A Gen.* 2011;396:159.
76. Martins RL, Baldanza MAS, Alberton AL, Vasconcelos SM, Schmal M. *Appl Catal B Environ.* 2011;103:326.
77. Martins RL, Schmal M. *Appl Catal A Gen.* 2006;308:133.
78. Muradov NZ. *Energy Fuels.* 1998;12:41.
79. Poirier MG, Sapundzhiev C. *Int J Hydrogen Energy.* 1997;22:429.
80. Choudhary TV, Goodman DW. *Catal Lett.* 1999;59:93.
81. Aiello R, Fiscus JE, zur Loye H-C, Amiridis MD. *Appl Catal A.* 2000;192:227.
82. Alberton AL, Souza MMVM, Schmal M. *Appl Catal B Environ.* 2011;103(3–4):326.
83. Li Y, Zhang B, Xie X, Liu J, Xu Y, Shen W. *J Catal.* 2006;238:412.
84. Ni X, Zhao Q, Zhou F, Zheng H, Cheng J, Li B. *J Crystal Growth.* 2006;289:299.
85. Zhu LP, Liao GH, Yang Y, Xiao HM, Wang JF, Fu SY. *Nanoscale Res Lett.* 2009;4:550.
86. Ni X, Zhang Y, Tian D, Zheng H, Wang X. *J Crystal Growth.* 2007;306:418.
87. Gui Z, Liv J, Wang Z, Song L, Hu Y, Fan W, Chen D. *J Phys Chem B.* 2005;109:119.
88. Winslow P, Bell AT. *J Catal.* 1985;94:385.
89. Duncan TM, Winslow P, Bell AT. *J Catal.* 1985;93:1.
90. Chorkendorff I, Alstrup I, Ullmann S. *Surf Sci.* 1990;227:291.
91. Egeberg RC, Ullmann S, Astrup I, Mullins CB, Chorkendorff I. *Surf Sci.* 2002;497:183.
92. Swang O, Faegri Jr K, Gropen O, Wahlgren U, Siegbahn P. *Chem Phys.* 1991;156:379.
93. Xing B, Pang X-Y, Wang G-C, Shang Z-F. *J Mol Catal A.* 2010;315:187.
94. Ribeiro NFP, Neto RCR, Moya SF, Souza MMVM, Schmal M. *Int J Hydrogen Energy.* 2010;35(21):11725–32.
95. Jeevanandam P, Kolytyn Y, Gedanken A. *Mater Sci Eng.* 2001;90:125–32.
96. Cui H, Zayat M, Levy D. *J Non-Cryst Solids.* 2005;351:2102–6.
97. Pompeo F, Gazzoli D, Nichio NN. *Int J Hydrogen Energy.* 2009;34:2260–8.
98. Han YS, Li JB, Ning XS, Yang XZ, Chi B. *Mater Sci Eng A.* 2004;369:241–4.
99. Guo J, Lou H, Zheng X. *Carbon.* 2007;45:1313–21.
100. Souza NA, Silva EB, Jardim PM, Sasaki JM. *Mater Lett.* 2007;61:4743–6.
101. Avgouropoulos G, Ioannides T, Matralis H. *Appl Catal B Environ.* 2005;56:87–93.
102. Patil KC, Aruna ST, Ekambaram S. *Combustion synthesis. Curr Opin Solid State Mater.* 1997;2:158–65.
103. Patil KC, Aruna ST, Mimani T. *Solid State Mater.* 2002;6:505–12.
104. Varma A, Rogachev AS, Mukasyan AS, Hwang S. *Adv Chem Eng.* 1998;24:79–226.
105. Kingsley JJ, Suresh K, Patil KC. *J Mater Sci.* 1990;25:1305–12.
106. Minami T. *J Alloy Compd.* 2001;315:123–8.
107. Alinejad B, Sarpoolaky H, Beitollahi A, Saberi A, Afshar S. *Mater Res Bull.* 2008;43:1188–94.
108. Chen Y, Zhou W, Shao Z, Xu N. *Catal Commun.* 2008;9:1318–25.
109. Ringuedé A, Labrincha JA, Frade JR. *Solid State Ion.* 2001;131:549–57.
110. Avgouropoulos G, Ioannides T. *Appl Catal A.* 2003;244:155–67.
111. Areán CO, Mentrui MP, López AJL, Parra JB. *Colloids Surf A.* 2001;180:253–8.
112. Sahli N, Roger AC, Kiennemann A, Libs S, Bettahar MM. *Catal Today.* 2006;113:187–93.
113. Han YS, Li JB, Ning XS, Chi B. *J Am Ceram Soc.* 2004;87:1347–9.
114. Hoffer BH, van Langeveld AD, Jannsens J-P, Bonné RLC, Martin C, Moulijn JA. *J Catal.* 2000;192:432–40.
115. Neto CRR, Schmal M. *Appl Catal A Gen.* 2013;450:131–2.

116. Mamontov E, Egami T, Brezny R, Koranne M, Tyagi S. *J Phys Chem B*. 2000;104:11110–6.
117. Khaodee W, Jongsomjit B, Assabumrungrat S, Praserttham P, Goto S. *Catal Commun*. 2009;10:494–501.
118. Reddy BM, Khan A. *Catal Surv*. 2005;9:155–71.
119. Su C, Li J, He D, Cheng Z, Zhu Q. *Appl Catal A*. 2000;202:81–9.
120. Postula WS, Feng Z, Philip CV, Akgerman A, Anthony RG. *J Catal*. 1994;135:126–31.
121. Feng Z, Postula WS, Akgerman A, Anthony RG. *Ind Eng Chem Res*. 1995;34:78–82.
122. Lu L, Hayakawa T, Ueda T, Hara M, Domen K, Maruya K. *Chem Lett*. 1998;1:65–6.
123. Maruya K, Takasawa A, Aikawa M, Haraoka T, Omen K. *J Chem Soc Faraday Trans*. 1994;90:911–7.
124. Zhu Z, He D. *Fuel*. 2008;87:2229–35.
125. Trovarelli A. *J Inorg Chem*. 1999;20:263–84.
126. Sun C, Li H, Chen L. *J Phys Chem Solids*. 2007;68:1785–90.
127. Sun C, Sun J, Xiao G, Zhang H, Qiu X, Li H, Chen L. *J Phys Chem B*. 2006;110:13445–52.
128. Sing KSW, Everett DH, Haul RAW, Moscou L, Pierotti RA, Rouquerol J, Siemieniowska T. *Pure Appl Chem*. 1985;57:603–19.
129. Nguyen C, Do DD. *Langmuir*. 1999;15:3608–15.
130. Donohue MD, Aranovich GL. *J Colloids Interf Sci*. 1998;205:121–30.
131. Leofanti G, Padovan M, Tozzola G, Venturelli B. *Catal Today*. 1998;41:207–19.
132. Burgess CGV, Everett DH, Nuttall S. *Pure Appl Chem*. 1989;61(11):1845–52.
133. Yuan Z, Idakiev V, Vantomme A, Tabakova T, Ren T, Su BL. *Catal Today*. 2008;131:203–10.
134. Bonnetot B, Rakic V, Yuzhakova T, Guimon C, Auroux A. *Chem Mater*. 2008;20:1585–96.
135. Aguila G, Guerrero S, Gracia F, Araya P. *Appl Catal A*. 2006;305:219–32.
136. Pérez-Hernández R, Aguilar F, Gómez-Cortés A, Díaz G. *Catal Today*. 2005;107:175–80.
137. Zawadzki M. *J Alloys Compd*. 2008;454:347–51.
138. Tartaj P, Bomati-Miguel O, Rebolledo AF, Valdes-Solis T. *J Mater Chem*. 2007;17:1958–63.
139. Bumajdad A, Zaki MI, Eastoe J, Pasupulety L. *Langmuir*. 2004;20:11223–33.
140. Inoue M, Sato K, Nakamura T, Inui T. *Catal Lett*. 2000;65:79–83.
141. Stagg-Williams SM, Noronha FB, Fendley G, Resasco DE. *J Catal*. 2000;194:240–9.
142. Wang ZL, Feng X. *J Phys Chem B*. 2003;107:13563–6.
143. Giamello E. *Catal Today*. 1998;41:239–49.
144. Abi-aad E, Bechara R, Grimblot J, Aboukais A. *Chem Mater*. 1993;5:793–7.
145. Adamski A, Djéga-Mariadassou G, Sojka Z. *Catal Today*. 2007;119:120–4.
146. Wang JB, Tai YL, Dow WP, Huang T-J. *Appl Catal A*. 2001;218:69–79.
147. Appel LG, Eon JG, Schmal M. *Physica Status Solidi*. 1997;163:107–20.
148. Voorhoeve RJH, Johnson DW, Remeika JP, Gallagher PK. *Science*. 1977;195:827–33.
149. Vaz T, Salker AV. *Mater Sci Eng B*. 2007;133:81–4.
150. Tascón JMD, González-Tejuca L. *Z Phys Chem-Wiesbaden*. 1980;121:63–78.
151. Tascón JMD, González-Tejuca L. *Z Phys Chem-Wiesbaden*. 1980;121:79–93.
152. Royer S, Duprez D, Kaliaguine S. *Catal Today*. 2006;112:99–102.
153. Galasso FS. *Perovskites and high TC superconductors*. 1st ed. Chap. 1. Amsterdam: Gordon and Breach Sc. Publ.; 1990.
154. Nitadori T, Muramatsu M, Misono M. The valence control and catalytic properties of $\text{La}_2-x\text{Sr}_x\text{NiO}_4$. *Bull Chem Soc Jpn*. 1988;61:3831–7.
155. Ferri D, Forni L. Methane combustion on some perovskite-like mixed oxides. *Appl Catal B*. 1998;16(2):119–26.
156. Spinicci R, Tofanari A, Faticanti M, et al. Hexane total oxidation on LaMO_3 (M = Mn, Co, Fe) perovskite-type oxides. *J Mol Catal A Chem*. 2001;176:247–52.
157. Quinelato AL, Longo ER, Leite MI, et al. Synthesis and sintering of ZrO_2CeO_2 powder by use of polymeric precursor based on Pechini process. *J Mater Sci*. 2001;36:3825–30.
158. Popa M, Kakihana M. Synthesis of lanthanum cobaltite (LaCoO_3) by the polymerizable complex route. *Solid State Ion*. 2002;151(1–4):251–7.

159. Villoria JA, Alvarez-Galvan MC, Navarro RM, et al. Zirconia-supported LaCoO₃ catalysts for hydrogen production by oxidative reforming of diesel: optimization of preparation conditions. *Catal Today*. 2008;138(3–4):135–40.
160. Machado BF, Serp P. *Catal Sci Technol*. 2012;2:54–75.
161. Geim AK, Novoselov KS. *Nat Mater*. 2007;6:183–91.
162. Chen D, Tang L, Li J. *Chem Soc Rev*. 2010;313:3157–80.
163. Brownson DAC, Kampouris DK, Banks CE. *J Power Sources*. 2011;1136:4873–85.
164. Novoselov KS, Geim AK, Morozov SV, Jiang D, Zhang Y, Dubonos SV, Grigorieva IV, Firsov AA. *Science*. 2004;306:666–9.
165. Singh V, Joung D, Zhai L, Das S, Khondaker SI, Seal S. *Prog Mater Sci*. 2011;56:1178–271.
166. Moussa SO, Panchakarla LS, Ho MQ, El-Shall MS. *ACS Catal*. 2013;4:535–45.
167. Hofmann U, Frenzel A. *Kolloid-Zeitschrift and Zeitschrift fur Polymere*. 1934;68:99–151.
168. Stankovich S, Dikin DA, Piner RD, Kohlhaas KA, Kleinhammes A, Jia Y, Wu Y, Nguyen ST, Ruoff RS. *Carbon*. 2007;45:1558–65.
169. Novoselov KS, Geim AK, Morozov SV, Jiang D, Katsnelson MI, Grigorieva IV, Dubonos SV, Firsov AA. *Nature*. 2005;438:197–200.
170. Lee C, Wei X, Kysar JW, Hone J. Measurement of the elastic properties and intrinsic strength of monolayer graphene. *Science*. 2008;321:385.
171. Ubbelohde AR, Lewis LA. *Graphite and its crystal compounds*. London: Oxford University Press; 1960.
172. Brodie BC. *Annales de Chime et de Physique*. 1860;513:466–72.
173. Staudenmaier L. *Chemische Berichte*. 1898;31:981–99.
174. Hummers WS, Offeman RE. *J Am Chem Soc*. 1958;80:939.
175. Hummers WS, Offeman RE. *J Am Chem Soc*. 1958;6:1339.
176. Salavagione HJ, Martínez G, Ellis G. *Macromol Rapid Commun*. 2011;32:1771–89.
177. Li X, Wang X, Zhang L, Lee S, Dai H. Chemically derived, ultrasmooth graphene nanoribbon semiconductors. *Science*. 2008;319:1229.
178. Saner B, Okyay F, Yürüm Y. *Fuel*. 2010;89:1903–10.
179. Schniepp HC, Li J-L, McAllister MJ, Sai H, Herrera-Alonso M, Adamson DH, Prud'homme RK, Car R, Saville DA, Aksay IA. *J Phys Chem B*. 2006;110:8535–9.
180. Slonczewski JC, Weiss PR. Band structure of graphite. *Phys Rev*. 1958;109:272.
181. McAllister MJ, Li JL, Adamson DH, Schniepp HC, Abdala AA, Liu J, Alonso MH, Milius DL, Car R, Prud'homme RK, Aksay IA. *Chem Mater*. 2007;19:4396–404.
- 181a. Schniepp HC, Abdala AA, Liu J, Alonso MH, Milius DL, Car R, Prud'homme RK, Aksay IA. *Chem Mater*. 2007;19:4396–404.
182. Zhang YB, Tan YW, Stormer HL, Kim P. Experimental observation of the quantum Hall effect and Berry's phase in graphene. *Nature*. 2005;438:201.
183. Alanyalioglu M, Segura JJ, Oró-Solè J, Casan-Pastor N. *Carbon*. 2012;50:92–152.
184. Balandin AA, Ghosh S, Bao W, Calizo I, Teweldebrhan D, Miao F, et al. Superior thermal conductivity of single-layer graphene. *Nano Lett*. 2008;8:1302.
185. Wu J, Becerril HA, Bao Z, Liu Z, Chen Y, Peumans P. Organic solar cells with solution-processed graphene transparent electrodes. *Appl Phys Lett*. 2008;92:263–302.
186. Li Y, Tang L, Li J. *Electrochem Commun*. 2009;11:846–9.
187. Ritter KA, Lyding JW. The influence of edge structure on the electronic properties of graphene quantum dots and nanoribbons. *Nat Mater*. 2009;8:235.
188. Thompson TE, Falardeau ER, Hanlon LR. The electrical conductivity and optical reflectance of graphite–SbF₅ compounds. *Carbon*. 1977;15:39.
189. Fuzellier H, Melin J, Herold A. Conductibilité électrique des composés lamellaires graphite–SbF₅ et graphite–SbCl₅. *Carbon*. 1977;15:45.
190. Shenderova OA, Zhirnov VV, Brenner DW. Carbon nanostructures. *Crit Rev Solid State Mater Sci*. 2002;27:227.
191. Krishnan A, Dujardin E, Treacy MMJ, Hugdahl J, Lynam S, Ebbesen TW. Graphitic cones and the nucleation of curved carbon surfaces. *Nature*. 1997;388:451.

192. Emtsev KV, Bostwick A, Horn K, Jobst J, Kellogg GL, Ley L, et al. Towards wafer-size graphene layers by atmospheric pressure graphitization of silicon carbide. *Nat Mater.* 2009;8:203.
193. Choi SM, Seo MH, Kim HJ, Kim WB. *Carbon.* 2011;49:904–9.
194. Sprinkle M, Siegel D, Yu Y, Hicks J, Tejada A, Taleb-Ibrahimi A, et al. First direct observation of a nearly ideal graphene band structure. *Phys Rev Lett.* 2009;103:226–803.
195. de Parga ALV, Calleja F, Borca BMCG, Passeggi J, Hinarejos JJ, Guinea F, et al. Periodically rippled graphene: growth and spatially resolved electronic structure. *Phys Rev Lett.* 2008;100:056807.
196. Zhang X, Li K, Li H, Lu J, Qiangang F, Chu Y. Graphene nanosheets synthesis via chemical reduction of grapheneoxide using sodium acetate trihydrate solution. *Synt Met.* 2013;193:132–8.
197. Park J, Mitchel WC, Grazulis L, Smith HE, Eyink KG, Boeckl JJ, Tomich DH, Pacley SD, Hoelscher JE. *Adv Mater.* 2010;2:4130–5.
198. Park J, Mitchel WC, Grazulis L, Smith HE, Eyink KG, Boeckl JJ, Tomich DH, Pacley SD, Hoelscher JE. *Adv Mater.* 2010;2:4140–5.
199. Li D, Muller MB, Gilje S, Kaner RB, Wallace GG. Processable aqueous dispersions of graphene nanosheets. *Nat Nanotechnol.* 2008;3:101.
200. He H, Riedl T, Lerf A, Klinowski J. *J Phys Chem.* 1996;100:19954–8.
201. Murray CB, Kagan CR, Bawendi MG. *Ann Rev Mater Sci.* 2000;30:545–610.
202. Araujo GC, Lima S, Rangel MC, Parola V, Peña MA, Fierro JLG. *Catal Today.* 2005;107:906–12.
203. Lee DW, Won JH, Shim KB. *Mat Lett.* 2003;57:3346–51.
204. Gajbhiye NS, Bhattacharya UE, Darshane VS. *Thermoc Acta.* 1995;264:219–30.
205. Ponce S, Peña MA, Fierro JLG. *Appl Catal B.* 2000;24:193–205.
206. Sis LB, Wirtz GP. *J Appl Phys.* 1973;44:5553–9.
207. Antolini E. *Mater Chem Phys.* 2003;78:563–73.
208. Antolini E. *Appl Catal B.* 2013;88:1–24.
209. Stankovic S, Dikin DA, Dommett GHB, Kohlhaas KM, Zimney EJ, Stach EA, Piner RD, Nguyen ST, Ruoff RS. *Nature.* 2006;442:282–6.
210. Sun Y, Wu Q, Shi G. *Energy Environ Sci.* 2011;4:1113–32.
211. Huang X, Yin Z, Wu S, Qi X, He Q, Zhang Q, Yan Q, Boey F, Zhang H. *Small.* 2011;7:1876–902.
212. Berger C, Song ZM, Li XB, Wu XS, Brown N, Naud C, Mayou D, Li T, Hass J, Marchenkov AN, Conrad EH, First PN, de Heer WA. *Science.* 2006;312:1191–8.
213. Dato A, Radmilovic V, Lee Z, Phillips J, Frenklach M. *Nano Lett.* 2008;8:2012–6.
214. Choucair M, Thordarson P, Stride JA. *Nat Nanotechnol.* 2009;4:30–3.
215. Liu N, Luo F, Wu H, Liu Y, Zhang C, Chen J. *Adv Funct Mater.* 2008;18:1518–25.
- 215a. Zhang X, Li K, Li H, Lu J, Qiangang F, Chu Y. *Synth Met.* 2014;193:132–8.
216. Wang G, Wang B, Park J, Wang Y, Sun B, Yao J. *Carbon.* 2009;47:3242–6.
217. Lee SH, Seo SD, Jin YH, Shim HW, Kim DW. *Electrochem Commun.* 2010;12:1319–22.
218. Lerf A, He H, Riedl T, Forster M, Klinowski J. *Solid State Ionics.* 1997;101–103:857–62.
219. Hontoria-Lucas C, Lopez-Peinado AJ, Lopez-Gonzalez JD, Rojas-Cervantes ML, Martin-Aranda RM. *Carbon.* 1995;33:1585–92.
220. Ramesha GK, Sampath S. *J Phys Chem C.* 2009;113:7985–9.
221. Wang Z, Zhou X, Zhang J, Boey F, Zhang H. *J Phys Chem C.* 2009;19:9071–5.
222. Dilimon VS, Sampath S. *Thin Solid Films.* 2011;519:2323–7.
223. Novoselov KS, Jiang Z, Zhang Y, Morozov SV, Stormer HL, Zeitler U, et al. Room-temperature quantum Hall effect in graphene. *Science.* 2007;315:979.
224. Sutter PW, Flege J, Sutter EA. Epitaxial graphene on ruthenium. *Nat Mater.* 2008;7:406.
225. Wintterlin J, Bocquet M-L. Graphene on metal surfaces. *Surf Sci.* 2013;603:1841.
226. Stankovich S, Dikin DA, Dommett GHB, Kohlhaas KM, Zimney EJ, Stach EA, et al. Graphene-based composite materials. *Nature.* 2006;442:282.

227. Verdejo R, Barroso-Bujans F, Rodriguez-Perez MA, de Saja JA, Lopez-Manchado MA. Functionalized graphene sheet filled silicone foam nanocomposites. *J Mater Chem*. 2008;18:2221.
228. Gilje S, Han S, Wang M, Wang KL, Kaner RB. A chemical route to graphene for device applications. *Nano Lett*. 2007;7:3394.
229. Gomez-Navarro C, Weitz RT, Bittner AM, Scolari M, Mews A, Burghard M, et al. Electronic transport properties of individual chemically reduced graphene oxide sheets. *Nano Lett*. 2007;7:3499.
230. Hummers WOR. Preparation of graphite oxide. *J Am Chem Soc*. 1958;80:939.
231. Paredes JI, Villar-Rodil S, Martinez-Alonso A, Tascon JMD. Graphene oxide dispersions in organic solvents. *Langmuir*. 2008;24:10560.
232. Negishi R, Hirano H, Ohno Y, Maehashi K, Matsumoto K, Kobayashi Y. *Thin Solid Films*. 2011;519:6447–52.
233. Jiao L, Zhang L, Wang X, Diankov G, Dai H. *Nature*. 2009;458:877–80.
234. Lotya M, Hernandez Y, King PJ, Smith RJ, Nicolosi V, Karlsson LS, Blighe FM, De S, Wang Z, McGovern IT, Duesberg GS, Coleman JN. *J Am Chem Soc*. 2009;131:3611–20.
235. Guo J, Ren L, Wang R, Zhang C, Yang Y, Liu T. *Compos B Eng*. 2011;42:290–5.
236. Liao KA, Mittal KA, Bose S, Leighton C, Mkhoyan K, Macosko CW. *ACS Nano*. 2011;5:1253–8.
237. Fan Z, Wang K, Wei T, Yan J, Song L, Shao B. *Carbon*. 2010;48:1686–9.
238. Mei X, Ouyang J. *Carbon*. 2011;49:5389–97.
239. Thakur S, Karak N. *Carbon*. 2012;50:5331–9.
240. Zhu C, Guo S, Fang Y, Dong S. *ACS Nano*. 2010;4:2429–37.
241. Shen J, Li T, Long Y, Shi M, Li N, Ye M. *Carbon*. 2012;50:2134–40.
242. Zangmeister CD. *Chem Mater*. 2010;22:5625–9.
243. Chen W, Yan L, Bangal PR. *J Phys Chem C*. 2010;113:19885–90.
244. Wang G, Shen X, Wang B, Yao J, Park J. *Carbon*. 2013;47:1359–64.
245. Zhu Y, Stoller MD, Cai W, Velamakanni A, Piner RD, David C, Ruoff RS. *ACS Nano*. 2010;2:1227–33.
246. Fan X, Peng W, Li Y, Li X, Wang S, Zhang G, Zhang F. *Adv Mater*. 2008;20:4490–3.
247. Lian P, Zhu X, Xiang H, Li Z, Yang W, Wang H. *Electrochim Acta*. 2010;56:834–40.
248. Kang X, Wang J, Wu H, Liu J, Aksay IA, Lin Y. *Talanta*. 2010;81:754–9.
249. Le LT, Ervin MH, Qiu HW, Fuchs BE, Lee WY. *Electrochem Commun*. 2011;13:355–8.
250. Xue X, Ma C, Cui C, Xing L. *Solid State Sci*. 2011;13:1526–30.
251. Liu C, Alwarappan S, Chen Z, Kong X, Li C. *Biosens Bioelectron*. 2010;25:1829–33.
252. Lemme MC, Echtermeyer TJ, Baus M, Szafranek BN, Bolten J, Schmidt M, Wahlbrink T, Kurz H. *Solid-State Electron*. 2008;52:514–8.
253. Zhang H, Zheng W, Yan Q, Yang Y, Wang J, Lu Z, Ji G, Yu Z. *Polymer*. 2010;51:1191–6.
254. Grande L, Chundi VT, Wei D, Bower C, Andrew P, Ryhänen T. *Particuology*. 2012;10:1–8.
255. Pantelic RS, Meyer JC, Kaiser U, Baumeister WF, Plitzko JM. *J Struct Biol*. 2010;170:152–6.
256. Chen W, Yan L, Bangal PR. *J Phys Chem C*. 2010;114:19885–90.
257. Wang G, Shen X, Wang B, Yao J, Park J. *Carbon*. 2009;47:1359–64.
258. Salas EC, Sun ZZ, Lüttge A, Tour JM. *ACS Nano*. 2010;4:4852–6.